Seismic modeling to monitor CO_2 geological storage: The Atzbach-Schwanenstadt gas field

Stefano Picotti,[1] José M. Carcione,[1] Davide Gei,[1] Giuliana Rossi,[1] and Juan E. Santos[2,3,4]

Received 3 June 2011; revised 18 April 2012; accepted 24 April 2012; published 8 June 2012.

[1] We develop a petro-elastical numerical methodology to compute realistic synthetic seismograms and analyze the sensitivity of the seismic response when injecting carbon dioxide (CO_2) in a depleted gas reservoir. The petro-elastical model describes the seismic properties of the reservoir rock saturated with CO_2, methane and brine, and allows us to estimate the distribution and saturation of CO_2 during the injection process. The gas properties, as a function of the in-situ pressure and temperature conditions, are computed with the Peng-Robinson equation of state, taking into account the absorption of gas by brine. Wave attenuation and velocity dispersion are based on the mesoscopic loss mechanism, which is simulated by an upscaling procedure to obtain an equivalent viscoelastic medium corresponding to partial saturation at the mesoscopic scale. Having the equivalent complex and frequency-dependent bulk (dilatational) modulus, we include shear attenuation and perform numerical simulations of wave propagation at the macroscale by solving the viscoelastic differential equations using the memory-variable approach. The pseudo-spectral modeling method allows general material variability and provides a complete and accurate characterization of the reservoir. The methodology is used to assess the sensitivity of the seismic method for monitoring the CO_2 geological storage at the Atzbach-Schwanestadt depleted gas-field in Austria. The objective of monitoring is the detection of the CO_2 plume in the reservoir and possible leakages of CO_2. The leakages are located at different depths, where the CO_2 is present as gaseous, liquid and supercritical phases. Even though the differences can be very subtle, this work shows that seismic monitoring of CO_2 from the surface is possible. While the identification of shallow leakages is feasible, the detection of the plume and deep leakages, located in the caprock just above the injection formation, is more difficult, but possible by using repeatability metrics, such as the normalized RMS (NRMS) images. Considering real-data conditions, affected by random noise, a reference detection threshold for deep leakages and the CO_2 plume in the reservoir corresponds to a signal-to-noise ratio of about 10 dB.

Citation: Picotti, S., J. M. Carcione, D. Gei, G. Rossi, and J. E. Santos (2012), Seismic modeling to monitor CO_2 geological storage: The Atzbach-Schwanenstadt gas field, *J. Geophys. Res.*, *117*, B06103, doi:10.1029/2011JB008540.

1. Introduction

[2] The emission of CO_2 to the atmosphere from the combustion of fossil fuels is one of the possible causes of the greenhouse effect. In order to avoid these emissions, one of the options is the geological storage of carbon dioxide in depleted hydrocarbon reservoirs or deep saline aquifers. An example of the latter is the Sleipner field in the North Sea [*Arts et al.* 2004; *Chadwick et al.*, 2010], where CO_2 is stored in the Utsira formation, a highly permeable porous sandstone 800 m below the sea bottom [*Fœrseth*, 1996; *Carcione et al.*, 2006].

[3] There are more saline aquifers than hydrocarbon reservoirs but they require more exploration because they have not been surveyed. The storage can be hydrodynamic as dissolved CO_2 in the formation waters. However, the storage should be made at supercritical pressures to avoid the presence of the gas phase. The best conditions start at a minimum depth of nearly 1 km (the critical pressure and temperature of CO_2 are 7.4 MPa and 31 °C, respectively). When CO_2 is stored into depleted oil and gas fields or unmineable coal seams, enhanced oil/gas recovery (EOR/EGR) and coal-bed methane production make CO_2 geological storage cost-effective [e.g., *Baines and Worden*, 2004].

[1]Istituto Nazionale di Oceanografia e di Geofisica Sperimentale, Sgonico, Italy.
[2]CONICET, Instituto del Gas y del Petróleo, Facultad de Ingeniería, Universidad de Buenos Aires, Buenos Aires, Argentina.
[3]Universidad Nacional de La Plata, La Plata, Argentina.
[4]Department of Mathematics, Purdue University, West Lafayette, Indiana, USA.

Corresponding author: S. Picotti, Istituto Nazionale di Oceanografia e di Geofisica Sperimentale, Borgo Grotta Gigante 42/c, I-34010 Sgonico, Italy. (spicotti@ogs.trieste.it)

Like EOR the effectiveness of EGR is be due to the pushing effect of the CO_2 cushion. However, while EOR is a well established technology, EGR is not yet common practice [e.g., *Oldenburg and Benson*, 2001; *Oldenburg*, 2003].

[4] Injection is already active in the K12-B gas-field [*Vandeweijer et al.*, 2006], offshore Netherlands, and in the Weyburn-Midale oil field [*Wilson and Monea*, 2004], located in southeast Saskatchewan, Canada. For all these options, a critical issue for geological storage is ensuring that the captured and stored CO_2 does not escape from the host formation during and after the injection. A key point, particularly when the site is onshore, is to provide confidence in predictions of the long-term location of CO_2 in the subsurface and to identify and measure any potentially hazardous leaks to the surface, requiring an efficient monitoring program.

[5] The choice among the wide range of available monitoring tools depends on the site characteristics, the objective and the costs [e.g., *Benson et al.*, 2004; *Arts and Winthaegen*, 2005]. Among the geophysical methods, the multichannel seismic methods (i.e. 3D/2D surface reflection seismics, vertical seismic profiling and cross-well seismics) provide, with the highest resolution, information about possible changes of the petro-elastical characteristics occurred in the storage zone. The effects of pore pressure on the frame of the host rock and the contrast between the acoustic properties of oil and brine and those of CO_2 are important factors. *Wang et al.* [1998] measured a pore pressure increase from 8 to 16 MPa due to CO_2 flooding at the McElroy field in West Texas. *Xue and Ohsumi* [2004] performed laboratory experiments and measured a P wave velocity change of 6 % caused by gaseous CO_2 injection and 10 % due to supercritical CO_2 injection. As noted by *Oldenburg* [2003], the density change of CO_2 is large in the transition from gaseous to supercritical conditions, and can approach that of liquid water. Instead, pure CH_4 (methane, hydrocarbon gas) exhibits no such drastic change. Also, the viscosity of CO_2 is low but always higher than the CH_4 viscosity. These variations may indicate that seismic methods can be used to monitor the presence and movement of the CO_2 plume into depleted oil and gas fields.

[6] In general, the sensitivity of the time-lapse (4D) seismic method depends on the survey plan (type of sources, number and location of receivers on the surface and/or well, etc.) and on the specific characteristics of the storage site [e.g., *Arts et al.*, 2004; *Chadwick et al.*, 2010]. It can be evaluated a priori through numerical modeling that takes into account the reservoir characteristics and storage process. These simulations allow to optimize the seismic surveys, which should be repeated over time to monitor the evolution of the injected CO_2. Seismic modeling is a suitable tool to image specific geological settings and to simulate different CO_2 geological storage scenarios, but its success depends on a correct description of the physical properties of the CO_2 bearing rocks.

[7] One of the main phenomena occurring in rocks, in particular partially saturated with gas, is the mesoscopic-loss effect. It has been shown that it is the major cause of P wave attenuation at seismic frequencies [e.g., *Pride et al.*, 2004]. It is caused by heterogeneities greater than the pore size but much smaller than the predominant wavelengths. A fast P wave traveling in a heterogeneous fluid-saturated porous material induces fluid-pressure gradients in the different regions of the medium. This in turn generates slow P waves that diffuse away from the interfaces separating the heterogeneities, causing energy loss and velocity dispersion. *Carcione and Picotti* [2006] and *Carcione* [2007] present a detailed physical description of this mechanism that it is present where there is any kind of mesoscopic heterogeneity. Because the mesoscopic-scale heterogeneities in the solid frame and fluid properties, typically on the order of centimeters, are much smaller than the wavelength, any finite element or finite difference numerical procedure based on Biot's equations is impractical. To overcome this difficulty, we present an alternative approach, based on an equivalent viscoelastic medium.

[8] This work investigates the sensitivity of the seismic properties to variations in CO_2 and CH_4 within a reservoir, as a feasibility study for future seismic time-lapse surveys. First, we define the fluid properties as a function of pressure and temperature, with the gas acoustic properties obtained from the real-gas Peng-Robinson equation of state (PR-EoS). We take into account the possibility that CH_4 and CO_2 can go into solution in the brine. This process affects the saturation of the gaseous phases and the density and bulk moduli of the liquid phases. Secondly, we obtain the dry-rock bulk and shear moduli as a function of porosity and clay content using the Hashin-Shtrikman theory and the Krief model [*Carcione et al.*, 2006]. Then, an equivalent complex dilatational modulus is determined by solving at the mesoscale local boundary value problems representing oscillatory compressibility tests on a representative volume of bulk material containing stochastic heterogeneities characterized by their statistical properties. Only heterogeneities in fluid properties are considered in this paper. The oscillations of these mesoscopic scale heterogeneous rock samples are assumed to obey Biot's equations of motion. The computed displacements allow us to determine the equivalent bulk modulus at the macroscale as functions of frequency. Moreover, by averaging over many realizations of the stochastic heterogeneities we obtain an average bulk modulus. The final viscoelastic model is obtained by fitting the computed modulus with a suitable viscoelastic causal model, i.e. the Zener model [e.g., *Carcione*, 2007], which is used to perform numerical simulations to obtain synthetic seismograms. *Picotti et al.* [2010] showed that mesoscopic models can effectively be approximated by using a Zener viscoelastic element. The anelasticity of shear waves is also described by the Zener model. Numerical simulations of wave propagation at the macroscale are performed in the time domain, using a single-phase viscoelastic algorithm, including wave attenuation [*Carcione*, 2007]. The advantages of this approach are that the use of very small grid spacings due to the presence of the Biot slow wave can be avoided, with a substantial computer memory saving. Moreover, the viscoelastic modeling algorithm uses fewer material properties and field variables than the corresponding poroelastic modeling, with further memory and computer time reduction. The numerical algorithm, based on the viscoelastic velocity-stress elastodynamic equations, uses a pseudospectral method. This approach allows the calculation of the spatial derivatives with high accuracy [*Carcione*, 2007].

[9] The numerical experiments illustrate the implementation of the methodology to compute synthetic seismograms with the purpose of studying the sensitivity of the seismic response under varying CO_2 saturations in the reservoir and

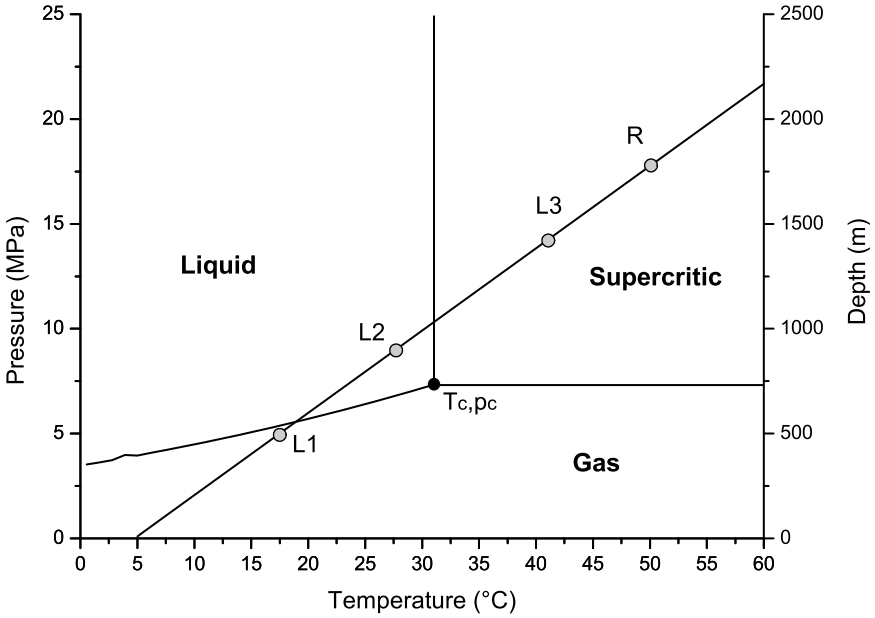

Figure 1. Phase diagram of CO_2 [*Mahan and Mayers*, 1987]. $T_c = 31.1^oC$ and $p_c = 7.38$ MPa are the CO_2 critical temperature and pressure, respectively. L1, L2 and L3 indicate the conditions of the three possible leakages considered in this work (see text for details).

for the detection of potentially hazardous leakages in the caprock and overburden. Note that for simplicity the term "leakage" is not used to indicate migration of CO_2 out of the storage complex, as formally specified in the European Directive, but rather to describe migration of CO_2 out of the reservoir. The methodology is applied to the Atzbach-Schwanenstadt gas field [*Polak et al.*, 2006], a potential site for underground CO_2 sequestration. This almost depleted gas-field, located in Upper Austria and operated by Rohoel-Aufsuchungs AG, is one of the four potential sites considered within the EU-funded CASTOR (CO_2 from CApture to STORage) project (2004–2008) [*Rossi et al.*, 2008]. Due to the presence of residual methane, the conditions for the seismic technique to map the CO_2 plume in the reservoir are less favorable than for a depleted oil reservoir or saline aquifer. Detection of leakages at early stages just above the injection formation is also very difficult, because the CO_2 can be present in the supercritical state. However, use of repeatability metrics such as the normalized RMS (NRMS [*Kragh and Christie*, 2002]) to assess the differences of repeated data sets increases the sensitivity of the seismic method, in particular if the monitoring is performed from the surface. Various scenarios have been considered, in order to model the seismic response of leakages containing CO_2 in different states (gaseous, liquid and supercritical states) and mixed with CH_4. The simulations confirm the suitability of the seismic method to monitor the evolution of the CO_2 plume in the reservoir and possible CO_2 leakages in the overburden and caprock.

1.1. Fluid Properties

[10] To correctly model the seismic response, it is necessary to calculate the physical properties of the fluids involved in the sequestration process. In this work, we consider brine and a mixture of methane and carbon dioxide. The fluid properties depend on temperature T and pressure p, which in turn depend on depth z. A simple – reference – situation is to consider a constant geothermal gradient, G, such that the temperature variation with depth is [*Carcione et al.*, 2006]

$$T = T_0 + Gz, \tag{1}$$

where T_0 is the average surface temperature and G is the average geothermal gradient (5 °C and 25 °C/km in our example, respectively). The pore pressure p at depth z depends on many factors, most of them of geological nature, such as low-permeability regions, sealing faults and hydrocarbons caps, which prevent pressure equilibration (communication) from the reservoir to the surface. The simplest case is when there are no permeability barriers and the fluids (say, water) are free to flow from depth z to the surface. In this case, the pore pressure is hydrostatic and is given by

$$p = \rho_b g z, \tag{2}$$

where ρ_b is the water (brine) density and g is the acceleration of gravity. With $\rho_b = 1$ gr/cm^3, the pore pressure ranges from 0 MPa at the surface to 30 MPa at 3 km depth. As shown in the CO_2 phase diagram of Figure 1 [*Mahan and Myers*, 1987], the injected CO_2 in the reservoir (R) is in the supercritical state.

[11] In-situ reservoir gas behaves as a real gas. In order to compute the density ρ_g of gases we consider the PR-EoS [*Peng and Robinson*, 1976], a cubic equation derived from the van der Waals equation (see Appendix A). Because of its simplicity and high performance, it is the most widely used EoS in chemical engineering thermodynamics. The bulk modulus of the gas K_g is given by [*Morse and Ingard*, 1986]

$$K_g = \gamma \rho_g \frac{\partial p}{\partial \rho_g}, \tag{3}$$

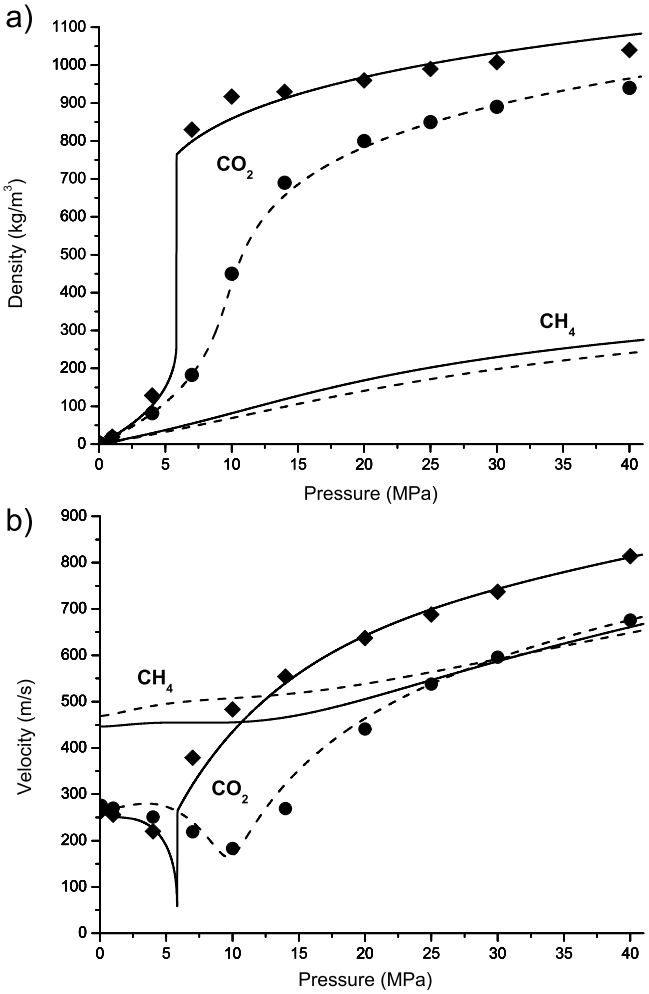

Figure 2. (a) Density and (b) sound velocity for CO_2 and CH_4 in the range of temperatures from 17°C to 47°C, and pressures from 0 to 40 MPa, considered in this work. Solid lines and dashed lines correspond to the isothermal curves of 17°C and 47°C, respectively. Diamonds and circles correspond to the CO_2 experimental data of *Wang and Nur* [1989].

where γ is the specific heat ratio. For air it is $\gamma = 3/4$. *Batzle and Wang* [1992] provide an empirical equation for the methane specific heat ratio:

$$\gamma = 0.85 + \frac{5.6}{p_r + 2} + \frac{27.1}{(p_r + 3.5)^2} - 8.7 \exp\left[-0.65(p_r + 1)\right], \quad (4)$$

where $p_r = p/p_c$ is the reduced pressure and p_c is the critical pressure. For CH_4, p_c = 4.64 MPa and for CO_2, p_c = 7.38 MPa. From a regression of the experimental data of *Wang and Nur* [1989], we obtain a similar empirical equation for the CO_2 specific heat ratio:

$$\gamma = 1.37 + \frac{11.29}{p_r + 6} + \frac{15.55}{(p_r + 1.3)^2} - 38.89 \exp\left[-1.25(p_r + 1)\right]. \quad (5)$$

[12] Figure 2 shows a comparison between the experimental data of *Wang and Nur* [1989] and the densities and sound velocities computed using the PR-EoS and the above equations. We observe an excellent agreement between the theoretical and experimental results in the temperature and pressure range considered in this work. Figure 2 shows also the corresponding theoretical plots for CH_4, which are in good agreement with those obtained using the empirical relations of *Batzle and Wang* [1992].

[13] The parameters of the CO_2-CH_4 mixtures are computed with the same relations used for pure components. However, in this case the parameters of the PR-EoS require a modification using the so-called mixing rules, which allow us to compute mixture parameters equivalent to those of pure substances (see Appendix A). The specific heat ratio of fluid mixtures is assumed to obey the same mixing rules used for the parameters of the PR-EoS [*Danesh*, 2001]:

$$\gamma = \gamma_1 x_1^2 + \gamma_2 x_2^2 + x_1 x_2 (\gamma_1 + \gamma_2), \quad (6)$$

where x_1, x_2 and γ_1, γ_2 are the molar fractions and the specific heat ratios of the two pure components, respectively. The viscosity of the pure components, as well as those of the fluid mixtures (as a function of pressure and temperature), is determined using the Lohrenz-Bray-Clark (LBC) theory [*Lohrenz et al.*, 1964].

[14] The brine acoustic properties depend on temperature, pressure and salinity. *Batzle and Wang* [1992] provide a series of useful empirical relations for density, velocity and viscosity. Using these relationships, we can also obtain the brine bulk modulus. Part of the hydrocarbon gas and CO_2 can dissolve in brine and the rest remain as free gas. There is a maximum quantity of gas that brine can absorb. *Carcione et al.* [2006] provide the equations to model the absorption of gas by brine. The mixture of free CO_2 and CH_4 with brine behaves as a composite fluid with properties depending on the stiffness moduli of the constituents and their respective saturations. The brine-fluid mixture density ρ_f is given by

$$\rho_f = S_g \rho_g + (1 - S_g)\rho_b, \quad (7)$$

where S_g is the free gas saturation and ρ_b is the brine density.

2. Formation Properties

[15] Because of the presence of clay and quartz, the grains are formed by a mixture of two solids and the effective grain moduli of the composite rock are different than the moduli of the single components. The density is simply

$$\rho_s = (1 - C)\rho_q + C\rho_c, \quad (8)$$

where ρ_q and ρ_c are the sand-grain (quartz) and clay densities, and C is the clay content. We assume that the grain bulk modulus K_s and shear modulus μ_s are equal to the arithmetic average of the upper and lower Hashin-Shtrikman bounds [*Hashin and Shtrikman*, 1963], as described in detail in *Carcione et al.* [2006]. When available, we use the P wave interval velocity c_P to compute the matrix bulk modulus K_m using the inverse Gassmann's equation [*Carcione et al.*, 2006]:

$$K_m = \frac{(\phi K_s/K_b + 1 - \phi)K_G - K_s}{\phi K_s/K_b + K_G/K_s - 1 - \phi}, \quad (9)$$

where ϕ is the porosity, K_b is the brine bulk modulus, $K_G = \rho c_P^2 - \frac{4}{3}\mu_m$ is the wet-rock (Gassmann) modulus, assuming the dry-rock shear modulus:

$$\mu_m = \frac{\mu_s}{K_s} K_m. \tag{10}$$

[16] If the P wave interval velocity is not available, we use Krief model:

$$K_m = K_s(1-\phi)^{A/(1-\phi)}, \tag{11}$$

where A is a dimensionless parameter. *Carcione et al.* [2005] verified that the value of $A = 3$ is appropriate for sediments composed by a mixture of quartz and clay. Clay content affects the permeability, which is not available for all the formations. *Carcione et al.* [2000] derived a model of permeability as a function of clay content. They assumed that a shaly sandstone is composed of a sandy matrix and a shaly matrix with partial permeabilities:

$$\kappa_q = \frac{R_q^2\phi^3}{45(1-\phi)^2(1-C)}, \quad \kappa_c = \frac{R_c^2\phi^3}{45(1-\phi)^2 C}, \tag{12}$$

where R_q and R_c denote the average radii of sand and clay particles, respectively. Assuming that permeability is analogous to the inverse of the electrical resistance, the average permeability of the shaly sandstone is given by

$$\frac{1}{\kappa} = \frac{1-C}{\kappa_q} + \frac{C}{\kappa_c} = \frac{(1-\phi)^2}{A\phi^3}\left[(1-C)^2 + C^2B^2\right], \tag{13}$$

where $A = R_q^2/45$ and $B = R_q/R_c$, or can be assumed as empirical parameters.

3. Modeling of Realistic Attenuation: Mesoscopic Loss

[17] The simulation of synthetic seismograms requires solving Biot's differential equations with very small grid spacings, since the loss mechanism involves the conversion of fast P wave energy to diffusion energy in the form of the Biot static mode. Because the wavelength of this mode can be very small, the poroelastic solution requires a very large amount of memory and computer time [*Picotti et al.*, 2007; *Rubino et al.*, 2007]. An efficient approach to overcome this problem is to compute the complex moduli of the equivalent viscoelastic medium and then solve the single-phase viscoelastic differential equations [*Carcione*, 1998; *Santos et al.*, 2008; *Picotti et al.*, 2010]. We consider a fluid-saturated porous material composed of several subdomains, and assume that the whole aggregate is isotropic. We also assume that some of the subdomains contain multiscale mesoscopic heterogeneities in the fluid properties, which are statistically homogeneous and can be described by their statistical properties. A representative volume element is denoted by Ω, and for simplicity let us assume that Ω is a square of side length L, i.e., $\Omega = (0, L)^2$. In the absence of external body sources, the oscillatory motion of Ω at the angular frequency ω is assumed to obey Biot's equations of motion, stated in the form [*Biot*, 1962; *Santos et al.*, 2009]

$$-\omega^2\rho u^s(\tilde{x},\omega) - \omega^2\rho_f u^f(\tilde{x},\omega) - \nabla\cdot\tau(u^s,u^f) = 0, \quad \tilde{x}\in\Omega, \tag{14}$$

$$-\omega^2\rho_f u^s(\tilde{x},\omega) - \omega^2\frac{S\rho_f}{\phi}u^f(\tilde{x},\omega) + \mathrm{i}\omega\frac{\eta}{\kappa}u^f(\tilde{x},\omega) + \nabla p_f(u^s,u^f) = 0, \quad \tilde{x}\in\Omega, \tag{15}$$

where $\mathrm{i} = \sqrt{-1}$, $\tilde{x}$ denotes the local coordinate system at the mesoscale in Ω, u^s and u^f are the solid and fluid relative to the solid displacement vectors, respectively, $\tau(u^s, u^f)$ is the total stress tensor and $p_f(u^s, u^f)$ is the fluid pressure. Also, ρ_s and ρ_f are the mass densities of the solid grains and of the saturating fluid and

$$\rho = (1-\phi)\rho_s + \phi\rho_f \tag{16}$$

is the bulk density of the material. Moreover, η is the fluid viscosity, κ the absolute permeability and S the structure or tortuosity factor. The stress-strain relations are [*Santos et al.*, 2009]

$$\tau_{jk}(u^s,u^f) = 2\mu\varepsilon_{jk}(u^s) + \delta_{jk}(\lambda_c\nabla\cdot u^s + \alpha M\nabla\cdot u^f), \tag{17a}$$

$$p_f(u^s,u^f) = -\alpha M\nabla\cdot u^s - M\nabla\cdot u^f, \tag{17b}$$

where $\varepsilon_{jk}(u^s)$ denotes the strain tensor and δ_{jk} is the Kronecker delta. The shear modulus of the bulk material μ is considered to be equal to the shear modulus of the dry matrix μ_m and $\lambda_c = K_G - \frac{2}{3}\mu$, with K_G being the Gassmann bulk modulus, i.e. the bulk modulus of the saturated material. The coefficients in (17a) and (17b) can be obtained from the relations

$$\alpha = 1 - \frac{K_m}{K_s}, \quad M = \left(\frac{\alpha-\phi}{K_s} + \frac{\phi}{K_f}\right)^{-1}, \quad K_G = K_m + \alpha^2 M, \tag{18}$$

where K_s, K_m and K_f denote the bulk moduli of the solid grains, dry matrix and saturant fluid, respectively. The viscoelastic model to be used at the macroscale to perform the numerical simulations is defined in terms of the (undrained) average equivalent dilatational modulus $\overline{K}_G(\omega)$. It is a complex and frequency-dependent modulus to be computed with Monte Carlo experiments, as described in detail in *Santos et al.* [2009]. Here, we briefly summarize the procedure. White's theory considers a simplified model for the gas distribution in the pore space, consisting of plane layers alternatively saturated by liquid and gas [*White et al.*, 1975], or spherical patches of gas in a background liquid [*White*, 1975]. Our methodology considers a more realistic medium consisting of fractal patches. Although the exact spatial distribution of these heterogeneities is in general unknown, they can be assumed to be stochastic functions characterized by their statistical properties. With this assumption, the idea is to average the properties over many patchy realizations of statistical parameters. To generate the quasi-fractal patchy saturated regions, we use a stochastic fractal field based on the so-called von Karman self-similar

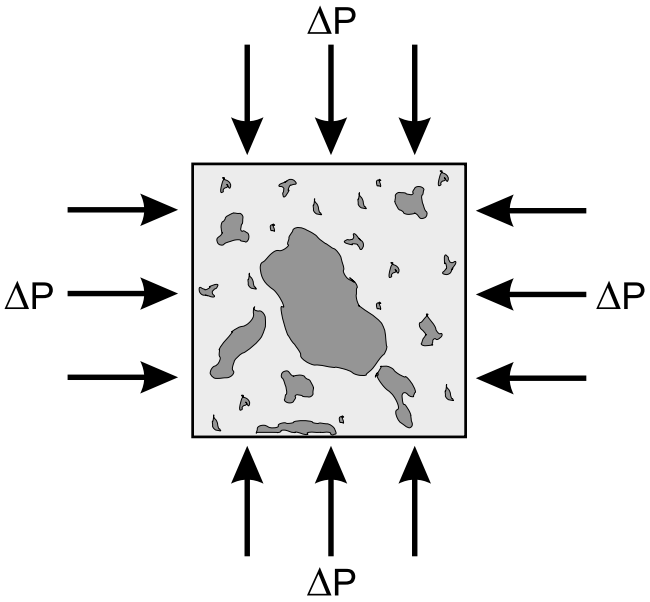

Figure 3. Schematic representation of the oscillatory compressibility test.

correlation functions. Following *Santos et al.* [2005], we consider a particular case for which the spectral density of the stochastic field is given by

$$S_d(k_x, k_y) = S_0(1 + k^2a^2)^{(s+n/2)}, \tag{19}$$

where $k = \sqrt{{k_x}^2 + {k_y}^2}$ is the radial wave number, a the correlation length, s is a self-similarity coefficient ($0 < s < 1$), n is the Euclidean dimension and S_0 is a normalization constant. Equation (19) corresponds to a fractal process of dimension $d = n + s - 1$ at scales smaller than a. Biot's equations (14) and (15) are solved over a set of realizations of representative samples Ω containing stochastic heterogeneities characterized by their statistical properties, with boundary conditions representing compressibility oscillatory tests at a finite number of frequencies. The size of the rock sample Ω is not arbitrary: it has to be large enough to constitute a representative volume of the medium but, at the same time, it has to be much smaller than the wavelengths associated with each excitation frequency. To obtain the equivalent complex P wave modulus $\overline{E}(\omega)$ associated with each realization of the reference sample, Ω is subjected to a time-harmonic compression of the form $\Delta P \exp(\mathrm{i}\omega t)$ on its top boundary, and no tangential forces are applied on the boundaries of the sample. Also, the solid is neither allowed to move on the bottom boundary nor to have horizontal displacements on the lateral boundaries, and the fluid is not allowed to flow in or out of the sample. Thus, we solved equations (14) and (15) with the following boundary conditions:

$$\begin{aligned} \tau(u^s, u^f)\nu &= (0, -\Delta P), \quad \text{on} \quad \Gamma^T, \\ \tau(u^s, u^f)\nu \cdot \chi &= 0, \quad \text{on} \quad \Gamma^L \cup \Gamma^R, \\ u^s \cdot \nu &= 0, \quad \text{on} \quad \Gamma^L \cup \Gamma^R, \\ u^s &= 0, \quad \text{on} \quad \Gamma^B, \\ u^f \cdot \nu &= 0, \quad \text{on} \quad \Gamma^L \cup \Gamma^R \cup \Gamma^B \cup \Gamma^T, \end{aligned} \tag{20}$$

where Γ^L, Γ^R, Γ^B and Γ^T are the left, right, bottom and top boundaries of Ω, respectively. In the expressions (20), ν is the unit outer normal and χ is a unit tangent oriented counterclockwise on the boundaries of Ω, such that $\{\nu, \chi\}$ is an orthonormal system on Γ. For a given realization of the stochastic parameters, the computed displacements on the top boundary Γ^T allow to measure the volume change of the sample, from where $\overline{K}_G(\omega)$ is determined as $\overline{E}(\omega) - (4/3)\mu_m$ [*Santos et al.*, 2009]. Figure 3 shows a schematic representation of an alternative undrained oscillatory compressibility test allowing a more direct computation of $\overline{K}_G(\omega)$.

[18] To solve equations (14) and (15) with (20) as boundary conditions we used a finite element procedure employing bilinear functions to approximate the solid displacement vector, while for the fluid displacement a closed subspace of the vector part of the Raviart-Thomas-Nedelec space of zero order is employed [*Raviart and Thomas*, 1975; *Nedelec*, 1980]. The mesh size used in this local problem, has to be small enough, that the diffusion process associated with the fluid pressure equilibration is accurately resolved. For practical purposes, in this work we take the mesh size so that the minimum diffusion length is discretized with at least three mesh points at the highest frequency, which is sufficient to represent a (smooth) diffusion-type process. See *Santos et al.* [2009] for details on the finite element spaces and mesh sizes used to solve each oscillatory local problem.

[19] The average and variance of the phase velocities and quality factors associated with these moduli are obtained by averaging over realizations of the stochastic parameters, and the Monte Carlo realizations are stopped when the variance of the computed quantities stabilize at an almost constant value. Once determined the average equivalent complex dilatational modulus $\overline{K}_G(\omega)$, the complex P wave velocity is given by

$$v(\omega) = \sqrt{\frac{\overline{K}_G(\omega) + (4/3)\mu_m}{\rho}}, \tag{21}$$

since the dry- and wet-rock shear moduli are the same, according to Gassmann's theory. The complex velocity has the following associated phase velocity and quality factor:

$$c = \left[\mathrm{Re}\left(\frac{1}{v}\right)\right]^{-1}, \tag{22}$$

$$Q = \frac{\mathrm{Re}(v^2)}{\mathrm{Im}(v^2)}, \tag{23}$$

respectively [e.g., *Carcione*, 2007]. In the next section, we approximate this medium by a viscoelastic equivalent medium and introduce shear wave attenuation.

4. Viscoelastic Representation of the Mesoscopic-Loss Mechanism

[20] The computed complex and frequency-dependent modulus $\overline{K}_G(\omega)$ must be approximated by a suitable causal viscoelastic model to compute synthetic seismograms in the time domain. Let us denote the fit of $\overline{K}_G(\omega)$ by $K(\omega)$. *Picotti et al.* [2010] showed that the mesoscopic model can be effectively approximated by using a Zener viscoelastic element. At sufficiently low frequencies, the fluid pressure

is uniform (iso-stress state) and the effective modulus of the pore fluid is given by Wood's equation [*Wood*, 1955]. We fit the real and imaginary parts of $\overline{K}_G$ with the corresponding viscoelastic ones by imposing the low-frequency limit $K(0) = \overline{K}_G(0) = K_G$, where K_G is given by equation (18), and

$$K_f = \left(\frac{1 - S_g}{K_b} + \frac{S_g}{K_g}\right)^{-1} \tag{24}$$

is the Wood average. Actually, imposing this condition, the only fitting parameter is the minimum dilatational quality factor $Q_0^{(1)}$ (see below).

[21] The complex moduli associated with bulk and shear deformations of a Zener element can be expressed as [*Carcione*, 2007]

$$M_\nu = \frac{1 + i\omega\tau_\epsilon^{(\nu)}}{1 + i\omega\tau_\sigma^{(\nu)}}, \quad \nu = 1, 2 \tag{25}$$

where $\tau_\sigma^{(\nu)}$ and $\tau_\epsilon^{(\nu)}$ are relaxation times. They are given by

$$\tau_\epsilon^{(\nu)} = \frac{\tau_0}{Q_0^{(\nu)}}\left(\sqrt{{Q_0^{(\nu)}}^2 + 1} + 1\right), \quad \tau_\sigma^{(\nu)} = \tau_\epsilon^{(\nu)} - \frac{2\tau_0}{Q_0^{(\nu)}}, \tag{26}$$

where τ_0 is a relaxation time such that $1/\tau_0$ is the center frequency of the relaxation peak and $Q_0^{(\nu)}$ are the minimum quality factors. In order to introduce shear dissipation, we assume that the complex modulus μ is described by a Zener element having a minimum quality factor given by

$$Q_0^{(2)} = \frac{\mu_m}{K_m} Q_0^{(1)}, \tag{27}$$

where $Q_0^{(1)}$ is the dilatational quality factor associated with K. The complex P and S wave moduli are then given by

$$\begin{aligned} E &= K + \frac{4}{3}\mu, \\ \mu &= \mu_m M_2, \end{aligned} \tag{28}$$

respectively, where

$$K = K_G M_1 \tag{29}$$

is the dilatational modulus. The complex P and S wave viscoelastic velocities are given by

$$v_P = \sqrt{\frac{E}{\rho}}, \quad v_S = \sqrt{\frac{\mu}{\rho}}, \tag{30}$$

and the respective phase velocities and quality factors are given by equations (22) and (23) but replacing v by v_P or v_S. The dilatational quality factor is

$$Q_1 = \frac{\mathrm{Re}(K)}{\mathrm{Im}(K)} = \frac{\mathrm{Re}(M_1)}{\mathrm{Im}(M_1)}, \tag{31}$$

whose minimum value as a function of frequency is $Q_0^{(1)}$ [e.g., *Carcione*, 2007].

5. Viscoelastic Differential Equations

[22] The time domain equations for propagation in a heterogeneous viscoelastic medium can be found in *Carcione* [2007]. The two-dimensional velocity-stress equations for anelastic propagation, considering the (x, z)-plane, are as follows:

[23] 1. Euler-Newton's equations:

$$\dot{v}_x = \frac{1}{\rho}(\sigma_{xx,x} + \sigma_{xz,z}) + f_x, \tag{32}$$

$$\dot{v}_z = \frac{1}{\rho}(\sigma_{xz,x} + \sigma_{zz,z}) + f_z, \tag{33}$$

where v_x and v_z are the particle velocities, σ_{xx}, σ_{zz} and σ_{xz} are the stress components, ρ is the bulk density (16) and f_x and f_z are the body forces. A dot above a variable denotes time differentiation.

[24] 2. Constitutive equations:

$$\dot{\sigma}_{xx} = K_u(v_{x,x} + v_{z,z} + e_1) + \mu_u(v_{x,x} - v_{z,z} + e_2), \tag{34}$$

$$\dot{\sigma}_{zz} = K_u(v_{x,x} + v_{z,z} + e_1) - \mu_u(v_{x,x} - v_{z,z} + e_2), \tag{35}$$

$$\dot{\sigma}_{xz} = \mu_u(v_{x,z} + v_{z,x} + e_3), \tag{36}$$

where e_1, e_2 and e_3 are memory variable and K_u and μ_u are the unrelaxed (high-frequency) bulk and shear moduli, respectively, given by

$$\begin{aligned} K_u &= K_G M_1(\infty) = K_G \tau_\epsilon^{(1)}/\tau_\sigma^{(1)}, \\ \mu_u &= \mu_m M_2(\infty) = \mu_m \tau_\epsilon^{(2)}/\tau_\sigma^{(2)}. \end{aligned} \tag{37}$$

[25] 3. Memory variable equations:

$$\dot{e}_1 = \left(\frac{1}{\tau_\epsilon^{(1)}} - \frac{1}{\tau_\sigma^{(1)}}\right)(v_{x,x} + v_{z,z}) - \frac{e_1}{\tau_\sigma^{(1)}}, \tag{38}$$

$$\dot{e}_2 = \left(\frac{1}{\tau_\epsilon^{(2)}} - \frac{1}{\tau_\sigma^{(2)}}\right)(v_{x,x} - v_{z,z}) - \frac{e_2}{\tau_\sigma^{(2)}}, \tag{39}$$

$$\dot{e}_3 = \left(\frac{1}{\tau_\epsilon^{(2)}} - \frac{1}{\tau_\sigma^{(2)}}\right)(v_{x,z} + v_{z,x}) - \frac{e_3}{\tau_\sigma^{(2)}}. \tag{40}$$

[26] The differential equations are solved with a 4th-order Runge-Kutta time stepping scheme and the staggered Fourier method for computing the spatial derivatives, which is noise-free in the dynamic range where regular grids generate artifacts that may have amplitudes similar to those of physical arrivals [*Carcione*, 2007].

6. Application to the Atzbach-Schwanenstadt Injection Site

[27] The Atzbach-Schwanenstadt gas field is one of the four test sites chosen by the EU co-funded CASTOR project to test and validate the technology [*Polak et al.*, 2006; *Rossi et al.*, 2008]. Rohoel-Aufsuchungs AG, which operates this field, tested its transformation into a CO_2 storage site as well as the suitability of CO_2 injection for EGR. Potential CO_2 sources would have been a paper mill (emitting about 0.2 Mt of CO_2 per year) and a fertilizer plant (emitting about 0.1 Mt

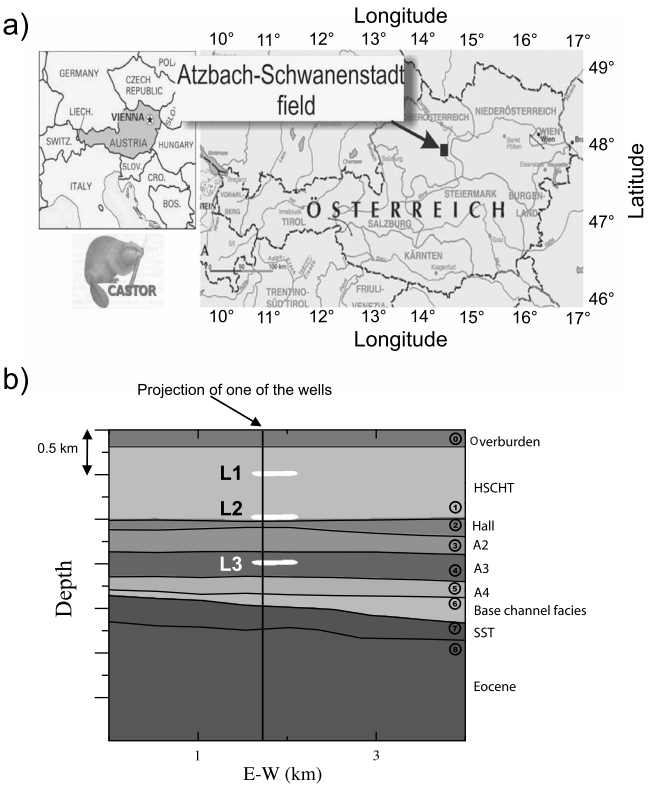

Figure 4. (a) Location of the Atzbach-Schwanenstadt gas-field, and (b) 2D section of the geological model. The main geological formations are indicated. It is assumed that CO_2 is injected in the reservoir, located in the A4 formation, at an average depth of about 1800 m, while the A3 formation is the caprock. L1, L2 and L3 indicate three possible leakages.

of CO_2 per year), while the transport of CO_2 would be ensured by trucks. The possible CO_2 injection rate could have been of about 0.2 Mt CO_2/year. CASTOR project studied the site assessment, encompassing the construction of a digital geological model and an upscaled reservoir model. Reservoir simulations carried out in these models allowed to evaluate the feasibility of an injection at 0.3 Mt CO_2/year for thirty years, starting from 2010, with and without EGR, and considering also new wells. The other project target was to investigate the effect of CO_2 injection on the mechanical stability of the site, and the risk for CO_2 migration to the groundwater or the atmosphere and the possibility of detecting CO_2 in such cases [*Polak et al.*, 2006]. This was guaranteed by soil gas measurements to provide background data for comparison to future soil gas monitoring, a feasibility study to assess the possibilities for seismic monitoring though the years, geochemical experiments and simulations to evaluate the effect of CO_2-rich brine on the reservoir seal, and finally, geomechanical experiments and simulations to assess the mechanical stability of the site [*Polak et al.*, 2006; *Le Thiez et al.*, 2009].

6.1. Geological Model

[28] The Atzbach-Schwanenstadt almost-depleted gas field is located in central northern Austria (Figure 4a), in the Molasse Basin in the foreland of the Alpine mountain chain, outside the area affected by compressional deformation. Molasse basin filling started from the latest Eocene to the early Oligocene. The reservoir sandstone intervals, approximately 1600 m below the surface, were formed in the Puchkirchen Basin, a deep water trough parallel to the Alpine front. The geological model (Figure 4b) has been built on the basis of seismic interpretation, geological knowledge, and well log data [*Polak et al.*, 2006], including the topographic surface and one low velocity layer to simulate the overburden.

[29] The model was then populated with the physical properties provided in part by the partners and in part from the existing literature [*Polak et al.*, 2006; *Rossi et al.*, 2008]. We revised all the parameters of *Rossi et al.* [2008]. Missing or unreliable parameters were computed using rock-physics theories (see section 2). The sedimentary sequence shows the presence of shaly sandstones with variable clay content from 30% to 50% (see Table 3). It is assumed that CO_2 is injected in the reservoir, located in the A4 formation at an average depth of about 1800 m (see Figure 4), while the overlying formation with high clay content constitutes the caprock.

[30] We consider three scenarios for the reservoir, described as follows. The first scenario represents the baseline, before the CO_2 injection, where the CH_4 saturation in the reservoir is 56% [*Polak et al.*, 2006]. The second scenario represents the reservoir half occupied by the CO_2 plume, and we assume that the CO_2 injection occurs at the bottom of the A4 formation (see Figure 4b). According to *Oldenburg and Benson* [2001], the CO_2 and CH_4 mixing would be limited because of the high density and viscosity of CO_2 relative to CH_4. Moreover, the relatively larger viscosity of CO_2 will make for a favorable mobility ratio displacement of CH_4 with diminished tendency to interfinger and mix with the displaced CH_4. Thus, a strong vertical density stratification is expected in the reservoir during and after CO_2 injection. Hence, we assume that the injected CO_2 replaces and displaces the in-situ CH_4 which, being less dense and viscous, migrates upward and is subjected to compression. Because of compression and a consequent further CH_4 production by EGR, we expect a decrease of CH_4 saturation. We assume a decrease of CH_4 saturation from 56% to 40%, after some years of CO_2 injection.

[31] Numerical simulations [*Oldenburg and Benson*, 2001] show that the mixed zone (where CO_2 and CH_4 are mixed together in equal proportions) after eight years is approximately 15 m thick, where mixing is due to molecular diffusion. Since CO_2 can be present in gaseous, liquid or supercritical states, and mixed with small amounts of CH_4, hereafter we will refer to these mixtures with the term *fluid.* Therefore, because of the density and viscosity difference between CO_2 and CH_4, we assume the presence of 90% CO_2 and 10% CH_4 at the bottom of the reservoir, pure CH_4 at the top, and a 15 m thick fluid mixture zone of CO_2 and CH_4 in equal proportions (50%) in the middle. The saturation of the fluid mixture at the bottom, having replaced the previously in-situ CH_4, should be 56%. The third scenario represents the reservoir fully saturated by a fluid mixture of 90% CO_2 and 10% CH_4.

[32] As shown in the geological model of Figure 4b, we simulate three possible leakage scenarios in a 2D model, caused by the degradation of the casing of an abandoned well. A realistic leakage scenario along a well with CO_2

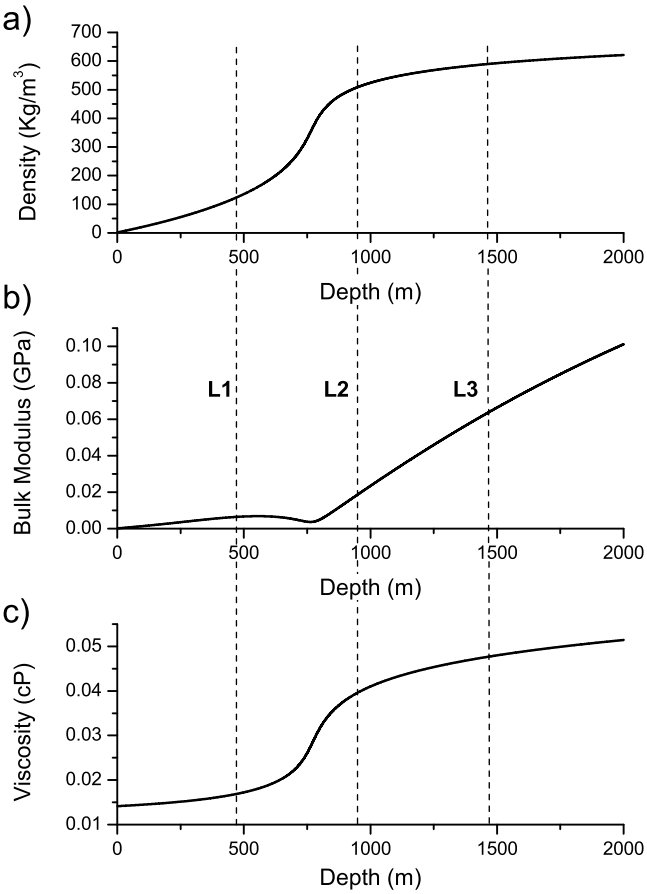

Figure 5. (a) Density, (b) bulk modulus, and (c) viscosity of a mixture composed of CO_2 (90%) and CH_4 (10%) versus depth. The three vertical dashed lines indicate the depth of the three considered leakages L1, L2 and L3.

accumulating in a shallow structure is probably not described by a 2D feature. However, the 2D approach is sufficient to demonstrate the basic principles of the specific problems considered in this study. In this work we simplified the geometry of the leakages, which is flat lying, to concentrate our efforts on modeling the seismic response of leakages containing CO_2 in different states (i.e., gaseous, liquid and supercritical). In fact, the state of CO_2 changes during its migration toward the surface, according to the changes in the pressure and temperature conditions defined by the CO_2 phase diagram (Figure 1). In any case, the flat lying geometry should not be considered a simplification in this kind of geological formations. In fact, they can be caused, for example, by the presence of thin layers with high clay content, which are common in sedimentary basins [*Chadwick et al.*, 2005, 2010]. These thin layers force the CO_2 to migrate horizontally. The leakages are composed by 90% CO_2 and 10% CH_4, which is the same fluid mixture present in the third reservoir scenario, with a saturation of 10%. The leakage size (in 2D) is approximately 500 m $\times$ 50 m. The reasoning behind the assumed saturation of only 10% is that the most important objective of monitoring is to detect small amounts of gas, i.e. CO_2 migrations at early stages. Considering the CO_2 phase diagram of Figure 1, the three leakages have the following characteristics: leakage 1 (L1) is located at 480 m depth, with the CO_2 in the gaseous state; leakage 2 (L2) is located at 950 m depth, with the CO_2 in the liquid state; leakage 3 (L3) is located at 1480 m depth, with the CO_2 in the supercritical state. Figure 5 shows the density (Figure 5a), bulk modulus (Figure 5b) and viscosity (Figure 5c) as a function of depth of the considered fluid mixture (90% of CO_2 and 10% of CH_4).

[33] Tables 1, 2 and 3 give the properties of the fluids, solids and formations constituting the model (see Figure 4b), respectively. Assuming for the leakages an elliptical geometry in the plain view, with a secondary axis of about 50 m, the three leakages contain about 15,300 m^3 (L1 and L2) and 10,000 m^3 (L3) of CO_2, which correspond to a total mass of about 2 kt (L1), 11.25 kt (L2) and 7 kt (L3) of CO_2. In Table 1, the brine has absorbed gas and f_0 indicates the peak frequency of the relaxation mechanism. The P wave velocities indicated in Table 3 are the experimental interval velocities used to obtain the dry-rock modulus (9), while c_S is obtained from Krief model (10) and the density (7).

[34] As explained in a previous section, we determine the equivalent complex bulk modulus solving at the mesoscale

Table 2. Grain Properties[a]

Medium	K (GPa)	μ (GPa)	ρ (kg/m^3)	R (μm)
Quartz[b]	36	45	2650	50
Clay[c]	12	6	2600	1

[a]Grain bulk modulus K, shear modulus μ, density ρ and average particle radius R.
[b]*Schön* [1996].
[c]*Wang et al.* [2001].

Table 1. Properties of the Leakages and Reservoir Fluids and Viscoelastic Parameters[a]

Medium	z (m)	S_g (%)	CO_2 (%)	CH_4 (%)	K_f (MPa)	ρ_f (kg/m^3)	η_f (cP)	K_b (GPa)	ρ_b (kg/m^3)	η_b (cP)	f_0 (Hz)	$Q_0^{(1)}$
						Leakage						
L1	480	10	90	10	6.53	128	0.017	2.43	1036	1.17	15	10.2
L2	950	10	90	10	18.8	509	0.04	2.6	1036	0.94	15	12.4
L3	1480	10	90	10	61.7	587	0.047	2.65	1035	0.77	15	45
						Reservoir						
R1	1800	56	0	100	36.3	128	0.018	2.7	1032	0.68	50	95
R2	1800	40	0	100	36.3	128	0.018	2.7	1032	0.68	30	62
R3	1800	56	50	50	47.1	295	0.028	2.7	1033	0.68	60	120
R4	1800	56	90	10	86.2	609	0.05	2.7	1034	0.68	80	150

[a]Average depth z, gas saturation S_g, percentage molar fraction of CO_2 and CH_4, fluid mixture bulk modulus K_f, density ρ_f and viscosity η_f, brine bulk modulus K_b, density ρ_b and viscosity η_b, peak frequency of the relaxation mechanism f_0 and corresponding dilatational quality factor $Q_0^{(1)}$.

Table 3. Formation Properties[a]

Formation	C (%)	ϕ (%)	κ (mD)	η_b (cP)	ρ (kg/m^3)	c_P (m/s)	c_S (m/s)	$Q_0^{(1)}$
Overburden	50	38	40	1.51	1827	800	400	50
HSCHT	30	26	42.6	1.11	2219	2600	1456	180
Hall	71	20	29.6	0.88	2298	3276	1890	260
A2	80	15	11	0.82	2373	3043	1710	210
A3	50	17	17	0.73	2353	3409	1984	240
A4	30	17	24.5	0.68	2362	3687	2365	165
Channel	40	15	15	0.65	2390	3752	2266	230
SST	50	15	15	0.63	2386	3200	1796	270
Eocene	50	15	15	0.57	2700	5200	2855	270

[a]Percentage clay content C, porosity ϕ, permeability κ, brine viscosity η_b, bulk density ρ, P wave velocity c_P and S wave velocity c_S. The baseline dilatational quality factors $Q_0^{(1)}$ correspond to the dominant frequency of 15 Hz.

(and for a finite number of frequencies) boundary value problems representing oscillatory compressibility tests on a representative volume of bulk material containing multiscale heterogeneities. Since the exact spatial distribution of these heterogeneities is in general unknown, they are assumed to be stochastic fractal fields based on the von Karman self-similar correlation functions (19). Figure 6 shows two different fluid patchy realizations, corresponding to the leakages (a), where the fluid saturation is 10%, and the reservoir (b), where the fluid saturation is 56%. In this case we used a side length of 50 cm, $d = 2.5$ and $a = 5$ cm as fractal dimension and correlation length, respectively.

[35] *Santos et al.* [2009] show that the variance of the equivalent compressional phase velocity averaged over the whole range of frequencies is stable after about 30 realizations. In our case, for the leakages, the variance is very small near the origin and around 0.01 and 10 m/s at 30 Hz, respectively for P wave attenuation and phase velocity. In the reservoir, at higher fluid mixture saturations, the variance reduces by an order of magnitude. Figures 7a–7d show the results obtained for the three leakages and reservoir. It is useful to compare these results with those obtained using White's layered model [*Carcione and Picotti*, 2006]. The period width used for the White model is 17 cm. The strong differences in the attenuation curves of Figure 7b justifies the use of the oscillatory tests, because White's model overestimates the attenuation. The results obtained for the reservoir show that the attenuation and velocity dispersion are lower than those obtained for the leakages. In particular, we observe that while the saturation of CH_4 decreases, the attenuation increases and the relaxation peak moves to lower frequencies. On the other hand, attenuation and velocity dispersion for the injected supercritical CO_2, which we assumed mixed with a small amount of CH_4 (10%), is very weak. The fact that leakages with 10% fluid mixture saturation have higher attenuation/dispersion than the reservoir scenarios is a result of oscillatory compressibility tests. However, this is also confirmed by White's model of patchy saturation. Using this model, *Carcione and Picotti* [2006] found that the most significant loss mechanisms are a result of porosity variations and partial saturation, where one of the fluids is very stiff and the other is very compliant. In particular, small amounts of free gas produce high attenuation and velocity dispersion effects, decreasing as free gas saturations increases. This phenomena can be intuitively understood by considering the energy transfer that occurs between the incident P wave and the

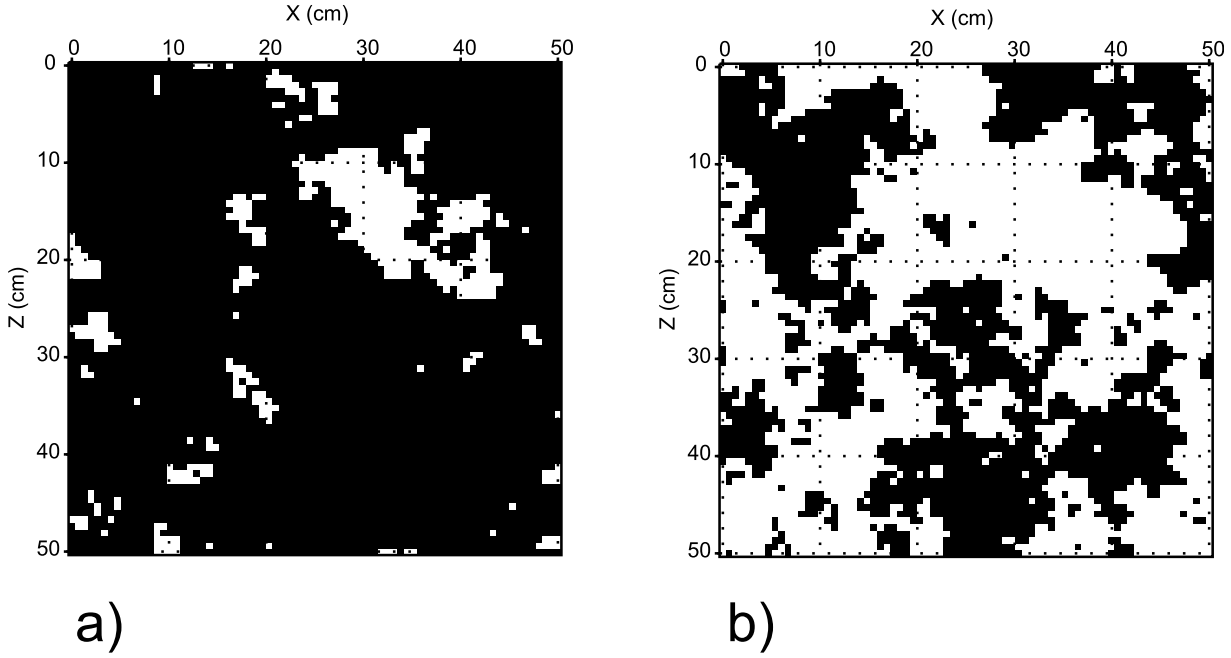

Figure 6. Two examples of fractal patchy realizations, corresponding to (a) the leakages (the fluid saturation is 10%), and (b) the reservoir (the fluid saturation is 56%). In these examples, white regions correspond to a fluid mixture composed by CO_2 (90%) and CH% (10%), and black regions to brine with absorbed gas.

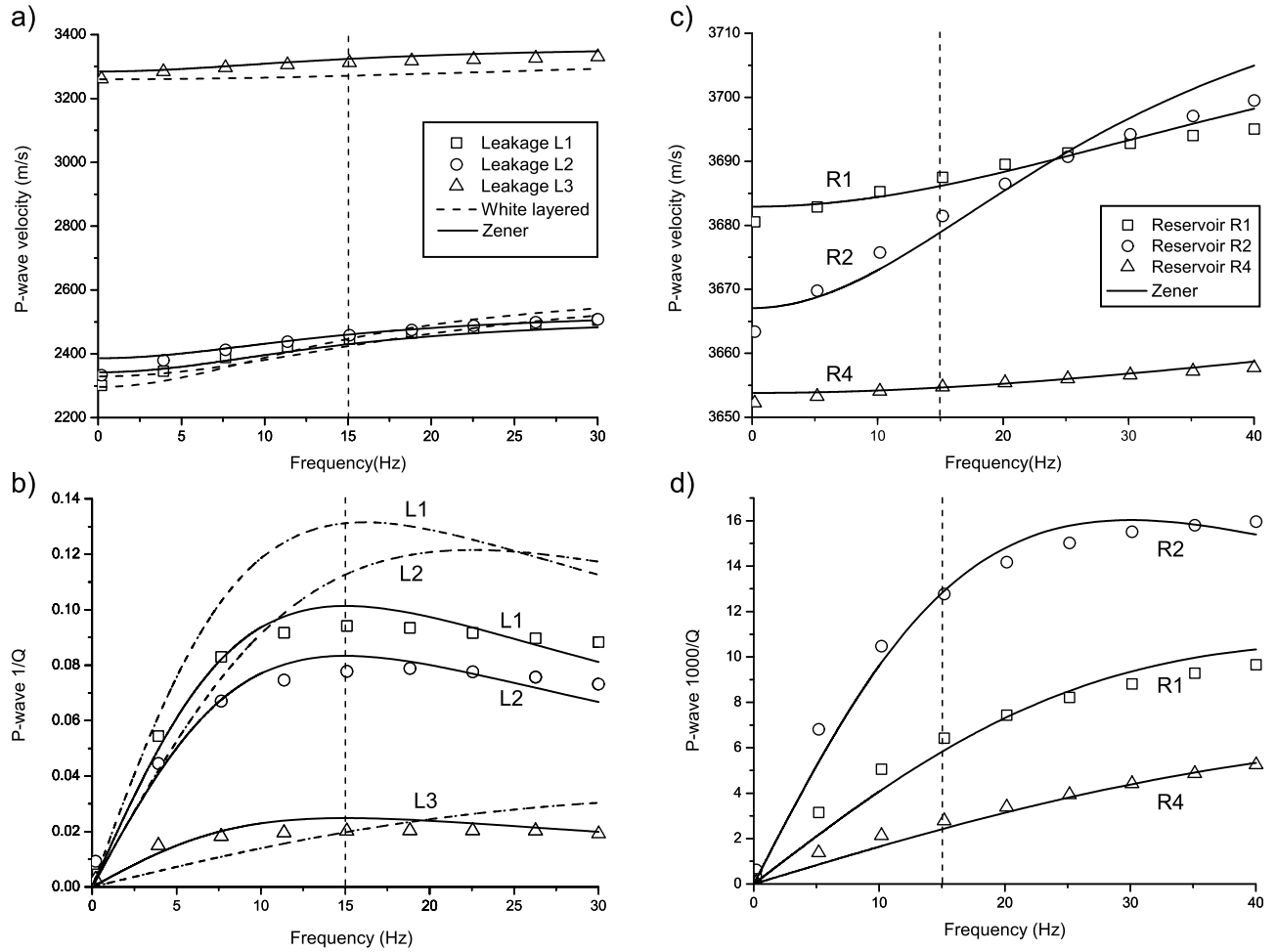

Figure 7. P wave velocity (Figures 7a and 7c) and quality factor (Figures 7b and 7d) obtained by using oscillatory compressibility tests. (a, b) The three leakages L1, L2, L3 are considered, (c, d) the reservoir formation saturated with pure CH_4 at 56% saturation (R1) and 40% saturation (R2), and with a mixture of CO_2 (90%) and CH_4 (10%) at 56% saturation (R4). Symbols represent numerical simulations (oscillatory compressibility tests at different frequencies), while solid lines represent the Zener model best fit. The parameters of the Zener model are then used for the viscoelastic numerical simulations in the time domain. Dashed lines in Figures 7a and 7b represent White's layered model using a period width of 17 cm. White's model overestimates attenuation.

diffused slow-wave. Higher saturation of the stiffest fluid means more bulk flow of fluid inside the pore space, which requires more energy to be supplied by the propagating wave, resulting in increased attenuation value. Obviously, at the limit of full saturation of the stiffest fluid, there is no attenuation because there is no compliant pore space where the fluid can move.

[36] Then, we define an equivalent viscoelastic model to be used for the computation of synthetic seismograms in the time domain. Figure 7 shows the Zener best fit of the P wave velocities and quality factors. Despite that the fits are not mathematically perfect, these results show that the Zener model provides a good approximation for practical purposes. We also use the Zener model for all the other formations by fitting the properties of the White plane-layered model and assuming a very small gas saturation of 0.1%. In the overburden, we assume brine and air in the pore space.

6.2. Synthetic Seismograms

[37] We simulated a 2D seismic acquisition corresponding to the model shown in Figure 4b. We used a grid composed of 800 $\times$ 720 points. The mesh has squared cells with a grid spacing of 5 m. This grid size is sufficient to sample the shortest wavelengths, according to the Nyquist theorem. We locate a receiver at every grid point at the surface and 102 sources 35 m spaced, to simulate a realistic seismic survey. The source is an explosion with a Ricker-wavelet time-history. The dominant frequency is 15 Hz, which corresponds to the attenuation peak frequency of the leakages (see Figure 7b). The wavefield is computed by using a time step of 0.5 ms till a maximum time of 2.2 s. We obtained imaging sections by applying the Kirchhoff pre-stack depth and time migration [*Yilmaz*, 1987] to the simulated seismograms. A gain function is applied during migration only to compensate for geometrical spreading. Common Imaging

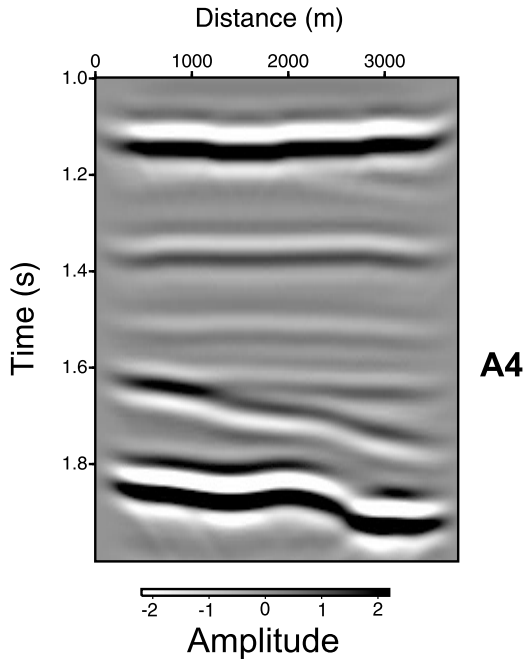

Figure 8. Magnification of the pre-stack time migration of the simulated baseline.

Gathers (CIG) are produced by the migration algorithm in order to find the best CIG stacking offset range and maximize the quality of the final imaging sections. Figure 8 shows a pre-stack time migration of the simulated seismograms corresponding to the baseline (first scenario), which can be compared to the real data published in *Rossi et al.* [2008]. Then, we migrated in depth the simulated seismograms after CO_2 injection, assuming that the velocity model has been refined, for example with a tomographic algorithm, to take into account the effect of the injected CO_2. Thus, any observed difference is attributed to changes in amplitude due to changes in attenuation and in the reflection coefficients.

[38] A useful procedure, when assessing the similarity of two time-lapse data sets, is to use repeatability metrics. Time-lapse repeatability is a key parameter controlling what can be detected seismically. One very common used metric is the normalized RMS (NRMS), where [*Kragh and Christie*, 2002]

$$\mathrm{NRMS} = 200\frac{\mathrm{RMS(repeat - base)}}{[\mathrm{RMS(repeat) + RMS(base)}]}. \qquad (41)$$

The NRMS, which is expressed as a percentage, varies radically in space and travel-time, and it is extremely sensitive to the smallest changes in the data. For example, a 10° phase shift, which is equivalent to 1.1 ms at 25 Hz, gives rise to a 17.4% NRMS residual. Figures 9a and 9b show the depth-migrated simulated seismograms before and after CO_2 injection, corresponding to the first and second scenarios. Figure 9c, representing the NRMS section obtained by using the migrated sections of Figures 9a and 9b, shows that the detection of the carbon dioxide in the reservoir is possible.

[39] We can clearly see that there is a difference between the pre-injection and post-injection phases, mainly concentrated in the bottom of the reservoir, because the second scenario represents the reservoir half saturated with CO_2, where the fluid mixture (90% CO_2 and 10% CH_4) accumulates at the bottom of the A4 formation. It indicates also the

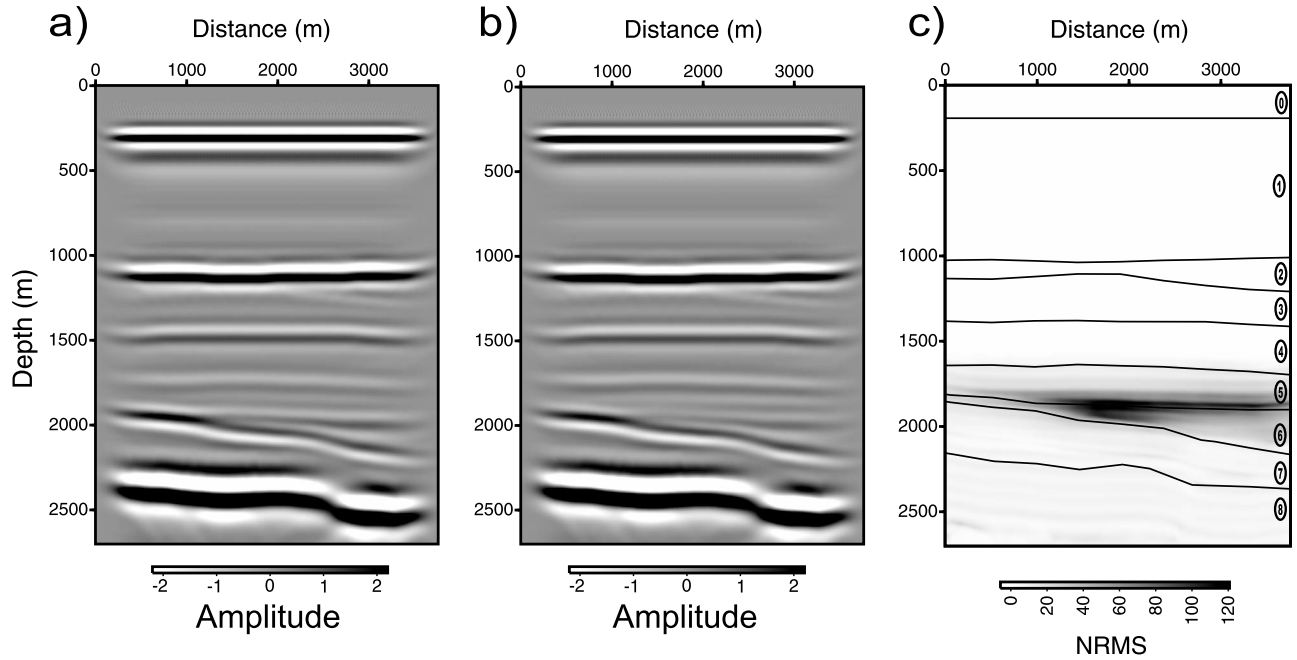

Figure 9. (a) Pre-stack depth migration of the simulated baseline, and (b) of the simulation assuming that half reservoir (A4 formation) is saturated with a mixture of CO_2 (90%) and CH_4 (10%). The CH_4 saturation is 56% in the first, and 40% in the second, while the mixture saturation is 56%. (c) The NRMS section obtained by using the simulations before and after the CO_2 injection clearly shows the effects of the presence of the CO_2 in the reservoir.

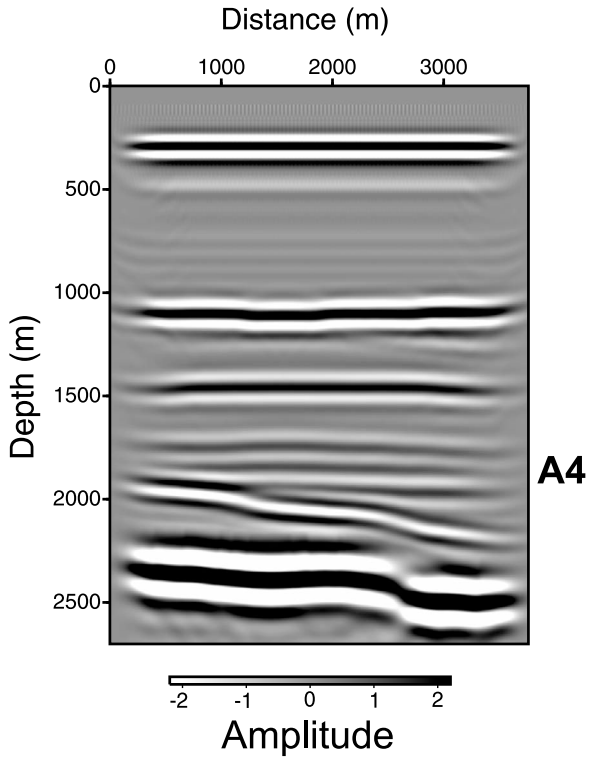

Figure 10. Pre-stack depth-migrated section related to the elastic simulation assuming that half reservoir is saturated with a mixture of CO_2 (90%) and CH_4 (10%), where in this case we do not consider the effect of attenuation (the quality factor is infinite in all the formations). This section has to be compared with the migrated section of Figure 9b, which represents the result of the corresponding viscoelastic simulation.

presence of a new weak reflection caused by the interface between gas layer R2 (methane) and R4 (mainly CO_2) in the middle of the reservoir.

[40] In order to show a clear picture of the attenuation effect, we carried out an elastic simulation of the second scenario. The corresponding depth-migrated section is shown in Figure 10. A comparison between this section and the corresponding viscoelastic section represented in Figure 9b, shows the impact of attenuation on the modeling. There is a noticeable difference in amplitude between these two sections and, due to the absence of velocity dispersion, in the elastic case the reflection events can easily be discriminated.

[41] Figures 11a and 11b show the depth-migrated simulated seismograms before and after CO_2 injection, related to the first and third scenarios, while Figure 11c shows the corresponding NRMS section. With respect to the previous case, the NRMS section shows lower NRMS residuals, but distributed on the whole reservoir area. This is plausible, because all the reservoir is saturated with CO_2. The higher NRMS residuals on the reservoir bottom of the second scenario are due to the presence of the new weak reflection discussed above. Moreover, as shown in Figure 7c, attenuation is higher for the gas layer R2 (methane) than for R4 (mainly CO_2). The average NRMS residual in the reservoir area is about 45%, which is comparable to the value of 35% reported by *Koster et al.* [2000] in Draugen Field, where they successfully observed brine replacing oil. Consider that, in the case of a depleted gas reservoir, the very subtle velocity differences might prevent a possible tomographic refinement of the interval velocity field to take into account the presence of CO_2. Therefore, the above NRMS residuals should be considered as lower limits, since the use of unrefined velocity fields in the migration should cast also differences in the spatial position of the reflectors (in particular at the reservoir bottom), increasing the NRMS residuals. In fact, the use of not refined velocity fields in the pre-stack depth migration would produce a pull-up effect at the reservoir bottom, because the velocity of the supercritical CO_2 is higher than the velocity of the replaced CH_4.

[42] Figures 12a–12c show the depth-migrated seismic sections after CO_2 injection (third scenario) in the presence of the leakages, to be compared with section 11b. With real seismic data, the most simple procedure to image possible leakages is to migrate the seismic data of repeated surveys using the interval velocity section obtained at the end of the injection phase. In this way, the presence of a leakage affects both traveltimes and amplitudes. The amplitude scale in Figure 12 clearly shows that these three type of leakages have different thresholds. As expected, the leakages L1 and L2, where CO_2 is respectively in the gaseous and liquid states, are easily identifiable, because of the strong impedance contrast. Therefore, notwithstanding the difficulties of the repeatability of a seismic survey onshore, possible CO_2 migration should be well detectable in the overburden.

[43] However, Figure 12a shows that detection of a leakage at early stage (L3) just above the injection formation (in the caprock), where CO_2 is still at the supercritical state, is very difficult. This is related to the state of CO_2 but also to the fact that leakage L3 is located in the caprock, which has a stiffer matrix and lower porosity than the formation HSCHT where the leakages L1 and L2 are located. A stiffer matrix would result in a smaller fluid effect than a softer rock. Again, the NRMS section obtained using the simulations before and after the leakage allows its detection. Figure 13a shows the NRMS footprint of leakage L3, where the average NRMS residual is about 50%. However, the differences are very subtle, and poor data quality can further reduce the detection sensitivity (presence of noise and/or non-repeatable acquisition patterns). In fact, repeatability depends mostly on time-lapse changes in ambient noise and in acquisition parameters. The former leads to random difference noise but the latter produces difference noise which depends systematically on baseline reflectivity. Repeatability also varies with depth. It is poorer at greater depths as signal penetration decreases, and also at shallow depths as fold decreases. These issues all affect what the time-lapse seismic can show at different levels. Here we study how the presence of random noise changes the NRMS signature of the deeper leakage L3, which is the most difficult to detect, assuming that the presence of this noise is the only factor controlling the repeatability. A complete treatment of repeatability requires also a rigorous modeling of acquisition patterns, which is beyond the aims of this paper. We contaminated the data with different amounts of random noise, in order to compute a detection threshold for this kind of leakage. A detection threshold can be expressed in terms of the signal-to-noise ratio, which is measured in

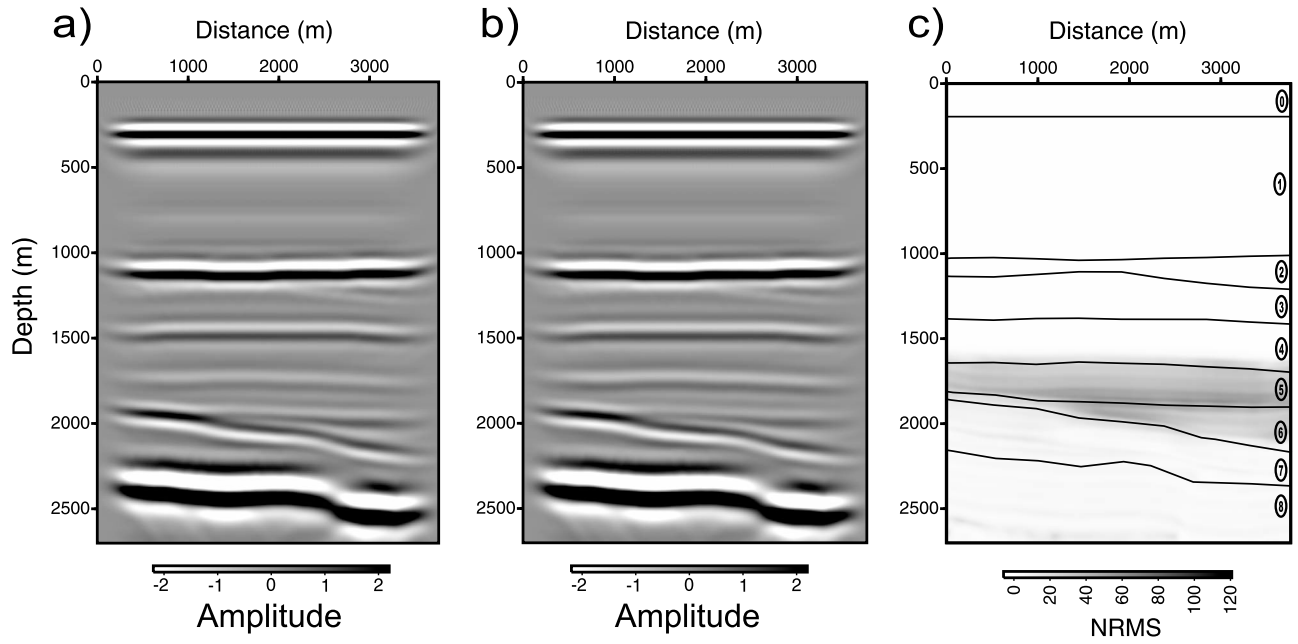

Figure 11. (a) Pre-stack depth migration of the simulated baseline, and (b) of the simulation assuming that the reservoir is fully saturated with a mixture of CO_2 (90%) and CH_4 (10%). The mixture saturation is 56%. (c) The NRMS section obtained by using the simulations before and after the CO_2 injection clearly shows the effects of the presence of the CO_2 in the reservoir.

decibel [*Sheriff and Geldart*, 1996]. In this case, the detection threshold of leakage L3 corresponds to a signal-to-noise ratio of about 10 dB (see Figure 13). In other words, a signal-to-noise ratio lower than 10 dB can prevent its detection. This conclusion is also valid for the third reservoir scenario, because it shows an average NRMS residual very similar to that of the leakage L3. Note that as the signal-to-noise ratio decreases, the average NRMS residual tends to the value of

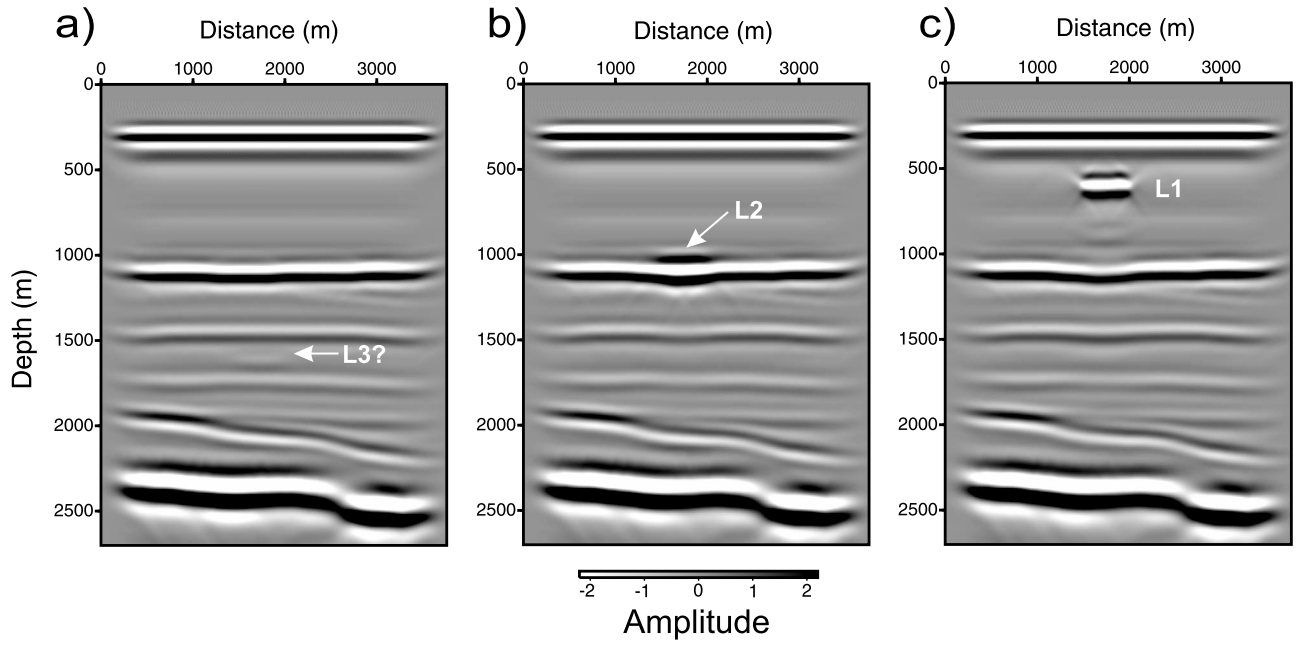

Figure 12. Pre-stack depth migration of the simulation after the CO_2 injection with leakage (a) L3, (b) L2, and (c) leakage L1. The leakages are composed of a mixture of CO_2 (90%) and CH_4 (10%), with a saturation of 10%. Leakages L1 and L2, with the CO_2 in the gaseous and liquid state respectively, are evident, while leakage L3, with the CO_2 in the supercritical state, is hardly resolved.

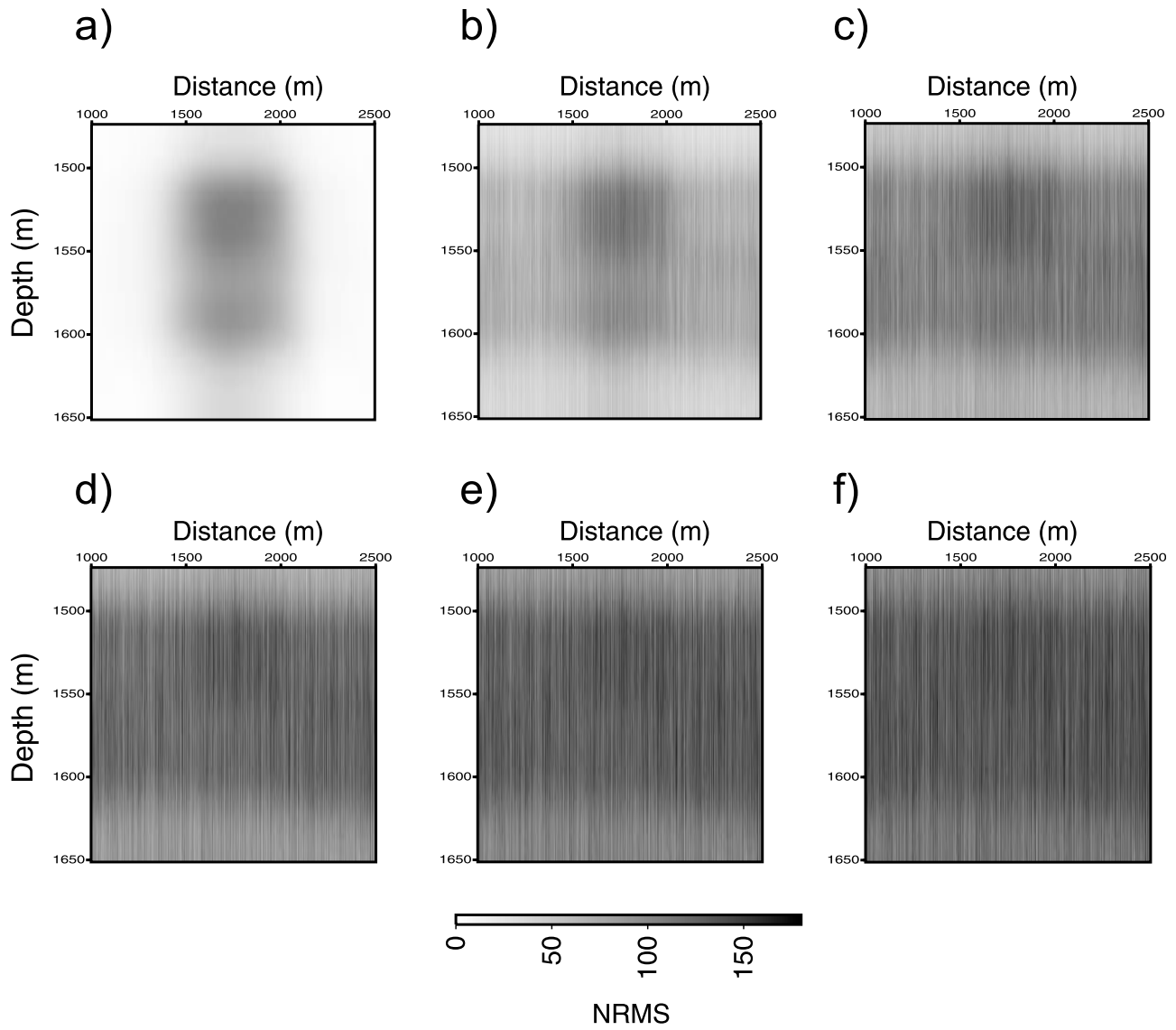

Figure 13. NRMS sections obtained by using the simulations after the CO_2 injection without leakages (Figure 11b) and the simulations after the CO_2 injection with only leakage L3 (Figure 12a). To simulate real data conditions, we contaminated the data with different percentages of random noise. In the panels, the signal-to-noise ratio is (a) ∞, (b) 20 dB, (c) 15 dB, (d) 10 dB, (e) 8 dB, and (f) 6 dB.

141% (see Figures 13d–13f), which corresponds to the theoretical NRMS value of traces containing only noise [*Kragh and Christie*, 2002].

[44] Finally, it should be noted that leakages can produce a velocity pushdown effect and an amplitude shadow effect on the reflected events below them. These effects are clearly evident in the pre-stack time migrated sections of Figure 14, where the details of the reflector below leakages L1 and L2 are shown. The velocity pushdown effect is also observable in the pre-stack depth-migrated sections (Figures 12b and 12c), because at the location of the leakages the seismic data are migrated using a velocity higher than it should be (we ignore the presence of leakages in the velocity field). These effects can easily be evaluated comparing the sections before and after the leakage. In the case of leakage L1 we have a maximum pushdown effect of about 5 ms and a lateral amplitude reduction of about 30% on the underlying reflector. Since leakages are generally small secondary accumulations with limited lateral extension, they produce seismic signals corresponding also to diffracted waves. Therefore, the amplitude shadow effect should be due to attenuation from scattering and mesoscopic loss, depending on the size of the leakage and the dominant frequency.

7. Discussion

[45] From Table 2, Table 3 and Figure 7 it follows that for shallow leakages, where the CO_2 is in the gaseous and liquid states, both P wave velocity and dilatational quality factors are very sensitive, while the sensitivity decreases significantly for deep leakages and the reservoir, where the CO_2 is in the supercritical state. S waves are less sensitive to the presence of CO_2 in the pore space. This is a consequence of the mesoscopic-loss effect, provided that the most

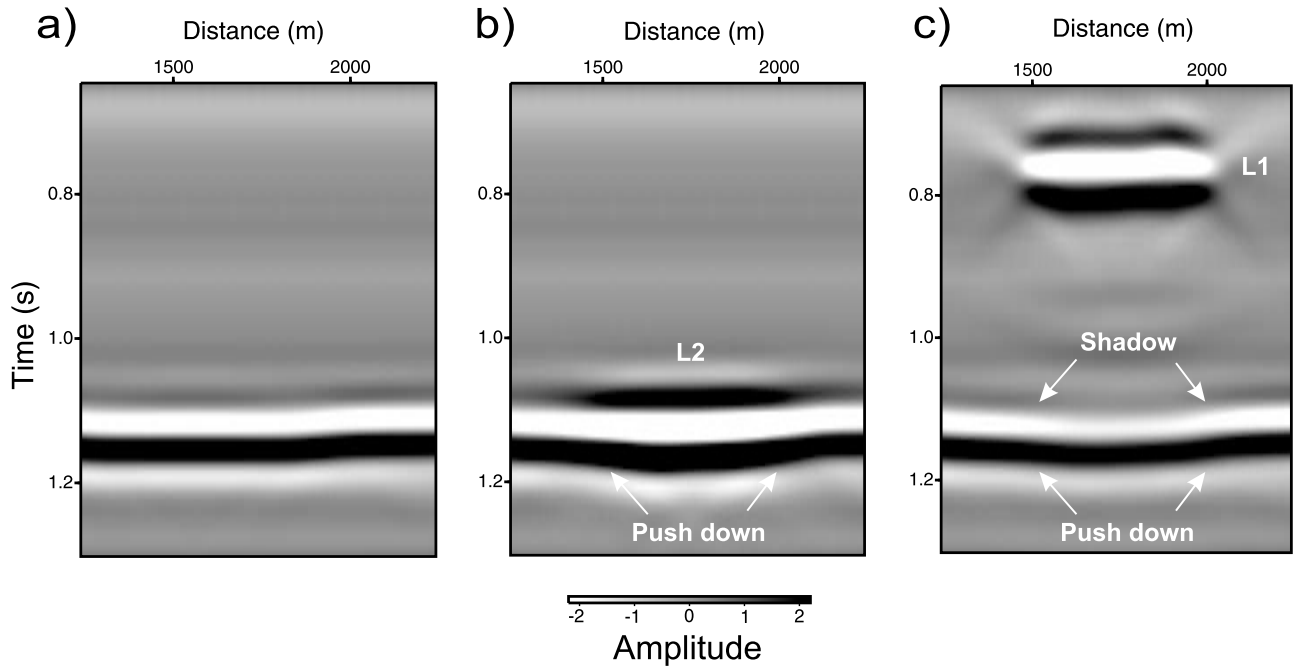

Figure 14. Pre-stack time migrations illustrating (a) the baseline, (b) the push down effect below the leakage L2 and (c) leakage L1.

significant loss mechanisms are a result of porosity variations and partial saturation, where one of the fluids is very stiff and the other is very compliant. In particular, small amounts of free gas produce high attenuation and velocity dispersion effects, decreasing as free gas saturations increases. The implications on a seismic monitoring plan oriented to the quantification of CO_2 accumulations are the following:

[46] 1. The acquisition pattern has to be accurately designed, so to guarantee a continuous and adequate coverage and a sufficient offset in order to obtain an accurate estimation of the interval velocity.

[47] 2. A seismic source with a wide frequency range is recommended to allow an accurate estimation of the quality factor.

[48] 3. 3C sensors are also recommended for multicomponent analyses, that represent an additional tool in order to better characterize the fluid content in the rocks.

[49] 4. If there is another gas in the reservoir (i.e. methane in the case of a depleted gas reservoir) and the saturation is high, the seismic response is small and it may be masked by noise. In this case, a cross-well seismic survey may help to better evaluate the changes within the reservoir, related to varying CO_2 saturations. It may also help to distinguish between CO_2 and CH_4 saturated zones.

[50] The methodology described in this work has global relevance. In fact, it can be applied elsewhere, in order to study the sensitivity of the seismic method to specific cases. From sensitivity studies it is possible to evaluate which seismic properties (P or S wave velocity or attenuation) show stronger variations in response to small CO_2 saturation variations, and tune the monitoring plan accordingly. The monitoring methods are site dependent since the results depend on the depth and in-situ conditions of the reservoir. Borehole monitoring, cross-well surveys, and a real-amplitude processing, are the key to obtain valuable results also in difficult situations. Leakage quantification requires a sufficient resolution, in order to correctly evaluate the leakage size, and knowledge of the petrophysical parameters of the formations. The pushdown effect, as described by *Chadwick et al.* [2005], allows an approximated estimation of the CO_2 saturation. Application of advanced tools such as travel-time and attenuation tomography based on the frequency-shift approach [*Böhm et al.*, 1999; *Rossi et al.*, 2007; *Picotti and Carcione*, 2006] will improve significantly the determination of the seismic velocity and quality factor. Together with rock-physics theories, these techniques can provide a more reliable quantification of the CO_2 accumulations.

8. Conclusions

[51] Time-lapse surface seismic technology represents a useful CO_2 monitoring technique during and after CO_2 injection, providing the temporal evolution of the CO_2 plume in the reservoir, and allowing the detection of possible dangerous leakages. In this work, we present a numerical methodology to obtain realistic synthetic seismograms in heterogeneous media, with the aim of assessing the sensitivity of the surface seismic method in the case of a depleted gas field, where CO_2 is stored. This methodology consists of rock-physics theories to calculate the properties of rocks and pore fluids, and in an upscaling procedure to obtain equivalent viscoelastic solids for heterogeneous fluid-saturated porous media. Oscillatory compressibility tests, based on a finite element solution of the classical Biot's equations in the space-frequency domain, enable us to obtain the equivalent complex and frequency-dependent bulk modulus of reservoir rocks. Since at mesoscopic scales the rock parameter distributions are generally uncertain and of stochastic nature, we apply the oscillatory tests based on Monte Carlo experiments. Then,

we approximate the Biot medium by an average equivalent viscoelastic solid based on the Zener model. This approach is computationally much less expensive than any numerical procedure based on the discretization of the full Biot's equations for the same order of accuracy.

[52] To illustrate the methodology, we built a petro-elastical model of the Atzbach-Schwanestadt almost depleted gas-field, located in Upper Austria, and computed synthetic seismograms. Different 2D rock models were considered, with the purpose of analyzing the sensitivity of the seismic response with varying saturations of CO_2 in the reservoir and for the detection of potentially hazardous leakages in the caprock and overburden, where the CO_2 can be present in three different states: gaseous, liquid and supercritical. The simulations show that these three type of leakages have different thresholds and are more evident when the CO_2 is present in the gaseous state, until about 600 m depth. However, they are also clearly visible when the CO_2 is present in the liquid state, until about 1100 m depth. On the contrary, detection of leakages at early stages (just above the reservoir, in the caprock) where the CO_2 is still present in the supercritical state, is more difficult. However, the use of repeatability metrics, such as the normalized RMS, when assessing the similarity of two repeated data sets, makes the time-lapse surface seismic technique suitable and more sensitive. A repeatability analysis of the simulated seismograms contaminated by random noise allowed us the computation of a reference detection threshold for this kind of leakages, which corresponds to a signal-to-noise ratio of about 10 dB. This is also valid for the reservoir, where the presence of another gas at high saturation makes the seismic response small and easy to be masked by background noise.

Appendix A: Density of the CO_2 - CH_4 Mixtures

[53] In-situ reservoir gas behaves as a real gas. The most common method used to compute the density ρ_g of real gases is to solve the equations of state. We consider the PR-EoS [*Peng and Robinson*, 1976]. This equation expresses the fluid properties in terms of the critical temperature T_c, the critical pressure p_c and the acentric factor ϖ:

$$p = \frac{RT}{V_m - b} - \frac{a\beta(\varpi)}{V_m{}^2 + 2bV_m - b^2}, \tag{A1}$$

where p is the gas pressure, V_m is the gas molar volume and R = 8.31 J/(mol °K) is the gas constant. If m is the mass of one mole of gas, then the gas density is $\rho = m/V_m$. For pure CH_4, m = 16 g/mole and ϖ = 0.0115, while for pure CO_2 it is m = 44 g/mole and ϖ = 0.225. For air it is m = 29 g/mole and ϖ = 0.078. Moreover,

$$\begin{aligned} a &= (0.45724R^2T_c^2)/p_c, \\ b &= (0.07780RT_c)/p_c, \\ \beta &= \left[1 + (0.37464 + 1.54226\varpi - 0.26992\varpi^2)\left(1 - \sqrt{T_r}\right)\right]^2, \end{aligned} \tag{A2}$$

where $T_r = T_a/T_c$ is the reduced temperature and $T_a = T(^oC) + 273.15$ is the absolute temperature. For CH_4, $T_c = -82.6^oC$, while for CO_2, $T_c = 31.1^oC$. The critical pressures for CH_4 and CO_2 are p_c = 4.64 MPa and p_c = 7.38 MPa, respectively. The gas density at the critical conditions, or critical density, is $\rho_c = 162.7$ kg/m^3 for CH_4 and $\rho_c = 468.2$ kg/m^3 for CO_2. For air it is $T_c = -140.8^oC$, p_c = 3.7 MPa and $\rho_c = 340$ kg/m^3.

[54] Earlier studies [*McQuarrie and Simon*, 1999] have shown that the PR-EoS exhibits performance similar to other EoS, like the Redlich-Kwong EoS and the Soave-Redlich-Kwong EoS [*Soave*, 1972], although it is generally better in predicting the densities of many species near the critical point, especially the non-polar ones. It also yields results comparable (and sometimes superior) to equations of higher complexity as the Valderrama-Patel-Teja EoS [*Valderrama*, 1990].

[55] The equations of state were developed for pure fluids first and then extended to mixtures. The mixture extension requires mixing rules, which allow us to obtain mixture parameters equivalent to those of pure substances. More precisely, the EoS parameters a and b in (A2) are expressed as functions of the parameters a_i and b_i and the concentration x_i of the pure components in the mixture

$$\begin{aligned} a &= \textstyle\sum_{i=1}^{N}\sum_{j=1}^{N} x_i x_j (1 - k_{ij})\sqrt{a_i a_j}, \\ b &= \textstyle\sum_{i=1}^{N}\sum_{j=1}^{N} x_i x_j \dfrac{b_i b_j}{2}, \end{aligned} \tag{A3}$$

where the binary interaction parameter k_{ij}, particularly useful in hydrocarbon mixtures with high concentration of CO_2, takes into account the attractive term between pairs of non-similar molecules [*Danesh*, 2001]. The above mixing rules, known as the van der Waals quadratic mixing rules, are used extensively in mixture calculations involving equations of state, and are well known to be suitable for hydrocarbon mixtures.

[56] **Acknowledgments.** The work was part of the EU funded CASTOR - CO_2, from capture to storage (contract SES6-CT-2004-502586, 2004–2008). We are indebted to the WP3.2 partners for helpful discussions, data exchange, and suggestions. We would like to thank Rohoel AG for their cooperation and support, and permission to present these results. We also thank the very useful suggestions of the reviewers.

References

Arts, R., and P. Winthaegen (2005), Monitoring options for CO_2 storage, in *Carbon Dioxide Capture for Storage in Deep Geologic Formations, Results From the CO_2 Capture Project*, vol. 2, edited by S. Benson, pp. 1001–1013, Elsevier, Oxford, U. K.

Arts, R., O. Eiken, R. A. Chadwick, P. Zweigel, L. Van der Meer, and B. Zinszner (2004), Monitoring of CO_2 injected at Sleipner using time-lapse seismic data, *Energy*, *29*, 1383–1392.

Baines, S. J., and R. H. Worden (2004), Geological storage of carbon dioxide, *Geol. Soc. Spec. Publ.*, *233*, 1–6.

Batzle, M., and Z. Wang (1992), Seismic properties of pore fluids, *Geophysics*, *57*, 1396–1408.

Benson, S., E. Hoversten, and E. Gasperikova (2004), Overview of monitoring techniques and protocols for geologic storage projects, *Greenhouse Gas R&D Programme Rep. PH4/35*, 108 pp., Int. Energy Agency, Paris.

Biot, M. A. (1962), Mechanics of deformation and acoustic propagation in porous media, *J. Appl. Phys.*, *33*, 1482–1498.

Böhm, G., G. Rossi, and A. Vesnaver (1999), Minimum time ray-tracing for 3-D irregular grids, *J. Seismol. Explor.*, *8*, 117–131.

Carcione, J. M. (1998), Viscoelastic effective rheologies for modeling wave propagation in porous media, *Geophys. Prospect.*, *46*, 249–270.

Carcione, J. M. (2007), *Wave Fields in Real Media: Wave Propagation in Anisotropic, Anelastic, Porous and Electromagnetic Media*, *Handb. Geophys. Explor.*, vol. 38, 2nd ed., 514 pp., Elsevier, Amsterdam.

Carcione, J. M., and S. Picotti (2006), P wave seismic attenuation by slow-wave diffusion: Effects of inhomogeneous rock properties, *Geophysics*, *71*, 1–8.

Carcione, J. M., B. Gurevich, and F. Cavallini (2000), A generalized Biot–Gassmann model for the acoustic properties of shaley sandstones, *Geophys. Prospect.*, *48*, 539–557.

Carcione, J. M., H. B. Helle, J. E. Santos, and C. L. Ravazzoli (2005), A generalized Gassmann modulus for multi-mineral porous media, *Geophysics*, *70*, N17–N26.

Carcione, J. M., S. Picotti, D. Gei, and G. Rossi (2006), Physics and seismic modeling for monitoring CO_2 storage, *Pure Appl. Geophys.*, *163*, 175–207.

Chadwick, R. A., R. Arts, and O. Eiken (2005), 4D seismic quantification of a growing CO_2 plume at Sleipner, North Sea, in *Petroleum Geology: North-West Europe and Global Perspectives - Proceedings of the 6th Petroleum Geology Conference*, edited by A. G. Dore and B. A. Vining, pp. 1385–1399, Geol. Soc., London.

Chadwick, R. A., et al. (2010), Quantitative analysis of time-lapse seismic monitoring data at the Sleipner CO_2 storage operation, *Leading Edge*, *29*, 170–177.

Danesh, A. (2001), *PVT and Phase Behaviour of Petroleum Reservoir Fluids*, Elsevier, Amsterdam.

Færseth, R. B. (1996), Interaction of Permo-Triassic and Jurassic extensional fault-blocks during the development of the Northern Sea, *J. Geol. Soc.*, *153*, 931–944.

Hashin, Z., and S. Shtrikman (1963), A variational approach to the theory of the elastic behaviour of multiphase materials, *J. Mech. Phys. Solids*, *11*, 127–140.

Koster, K., P. Gabriels, M. Hartung, J. Verbeek, G. Deinum, and R. Staplesc (2000), Time-lapse seismic surveys in the North Sea and their business impact, *Leading Edge*, *19*, 286–293, doi:10.1190/1.1438594.

Kragh, E., and P. Christie (2002), Seismic repeatability, normalized rms and predictability, *Leading Edge*, *21*, 642–647.

Le Thiez, P. (2009), CASTOR(CO2, CASTOR: CO2 from capture to storage, report, IFP Energ. Nouvelles, Rueil-Malmaison, France. [Available at http://www.cslforum.org/publications/documents/CASTOR_Final_Executive_Summary_CSLF.pdf.]

Lohrenz, J., B. G. Bray, and C. R. Clark (1964), Calculating viscosities of reservoir fluids from their compositions, *J. Pet. Technol.*, *16*, 1171–1176.

Mahan, B. H., and R. J. Myers (1987), *University Chemistry*, Benjamin Commings, Menlo Park, Calif.

McQuarrie, D. A., and J. D. Simon (1999), *Molecular Thermodynamics*, 656 pp., Univ. Sci. Books, Sausalito, Calif.

Morse, P. M., and K. U. Ingard (1986), *Theoretical Acoustics*, Princeton Univ. Press, Princeton, N. J.

Nedelec, J. C. (1980), Mixed finite elements in R^3, *Numer. Math.*, *35*, 315–341.

Oldenburg, C. M. (2003), Carbon dioxide as cushion gas for natural gas storage, *Energy Fuels*, *17*, 240–246.

Oldenburg, C. M., and S. M. Benson (2001), CO_2 injection for enhanced gas production and carbon sequestration, paper presented at International Petroleum Conference and Exhibition, Soc. Pet. Eng., Villahermosa, Mexico.

Peng, D. Y., and D. B. Robinson (1976), A new two-constant equation of state, *Ind. Eng. Chem. Fundam.*, *15*(1), 59–64.

Picotti, S., and J. M. Carcione (2006), Estimating seismic attenuation (Q) in the presence of random noise, *J. Seismol. Explor.*, *15*, 165–181.

Picotti, S., J. M. Carcione, J. G. Rubino, and J. E. Santos (2007), P wave seismic attenuation by slow-wave diffusion: Numerical experiments in partially saturated rocks, *Geophysics*, *72*, N11–N21.

Picotti, S., J. M. Carcione, J. G. Rubino, J. E. Santos, and F. Cavallini (2010), A viscoelastic representation of wave attenuation in porous media, *Comput. Geosci.*, *36*, 44–53.

Polak, S., et al. (2006), The Atzbach-Schwanenstadt gas field: A potential site for onshore CO_2 storage and EGR, *Leading Edge*, *25*, 1270–1275.

Pride, S. R., J. G. Berryman, and J. M. Harris (2004), Seismic attenuation due to wave-induced flow, *J. Geophys. Res.*, *109*, B01201, doi:10.1029/2003JB002639.

Raviart, P. A., and J. M. Thomas (1975), Mixed finite element method for 2nd order elliptic problems, in *Mathematical Aspects of the Finite Element Methods*, *Lect. Notes Math.*, vol. 606, pp. 292–315, Springer, New York.

Rossi, G., D. Gei, S. Picotti, and J. M. Carcione (2008), CO_2 storage at the Aztbach-Schwanenstadt gas field: A seismic monitoring feasibility study, *First Break*, *26*, 45–51.

Rubino, J. G., J. E. Santos, S. Picotti, and J. M. Carcione (2007), Simulation of upscaling effects due to wave-induced fluid flow in Biot media using the finite element method, *J. Appl. Geophys.*, *62*, 193–203.

Santos, J. E., C. L. Ravazzoli, P. Gauzellino, and J. M. Carcione (2005), Numerical simulation of ultrasonic waves in reservoir rocks with patchy saturation and fractal petrophysical properties, *Comput. Geosci.*, *9*, 1–27.

Santos, J. E., J. G. Rubino, and C. L. Ravazzoli (2008), Modeling mesoscopic attenuation in a highly heterogeneous Biot's medium employing an equivalent viscoelastic model, *SEG Exp. Abstr.*, *27*, 2112–2116.

Santos, J. E., J. G. Rubino, and C. L. Ravazzoli (2009), A numerical upscaling procedure to estimate effective bulk and shear moduli in heterogeneous fluid-saturated porous media, *Comput. Methods Appl. Mech. Eng.*, *198*, 2067–2077.

Schön, J. H. (1996), *Physical Properties of Rocks: Fundamentals and Principles of Petrophysics*, *Handb. Geophys. Explor.*, vol. 18, Pergamon, Oxford, U. K.

Sheriff, R. E., and L. P. Geldart (1996), *Exploration Seismology*, 592 pp., Cambridge Univ. Press, Cambridge, U. K.

Soave, G. (1972), Equilibrium constants from a modified Redlich-Kwong equation of state, *Chem. Eng. Sci.*, *27*, 1197–1203.

Valderrama, J. O. (1990), A generalized Patel-Teja equation of state for polar and non-polar fluids and their mixtures, *J. Chem. Eng. Jpn.*, *23*, 87–91.

Vandeweijer, V. P., L. G. H. Van der Meer, C. Hofstee, D. D'Hoore, and F. Mulders (2006), CO_2 Storage and Enhanced Gas Recovery at K12-B, paper presented at 71st Conference and Exhibition, Eur. Assoc. Geosci. Eng., Amsterdam.

Xue, Z., and T. Ohsumi (2004), Seismic wave monitoring of CO_2 migration in water-saturated porous sandstone, *Explor. Geophys.*, *35*, 25–32.

Wang, Z., and A. Nur (1989), Effect of CO_2 flooding on the velocities in rocks with hydrocarbons, *SPE Reservoir Eng.*, *4*, 429–436.

Wang, Z., M. Cates, and R. T. Langan (1998), Seismic monitoring of a CO_2 flood in a carbonate reservoir: A rock physics study, *Geophysics*, *63*, 1604–1617.

Wang, Z., H. Wang, and M. E. Cates (2001), Effective elastic properties of solid clays, *Geophysics*, *66*, 428–440.

White, J. E. (1975), Computed seismic speeds and attenuation in rocks with partial gas saturation, *Geophysics*, *40*, 224–232.

White, J. E., N. G. Mikhaylova, and F. M. Lyakhovitskiy (1975), Low-frequency seismic waves in fluid-saturated layered rocks, *Izv. Acad. Sci. USSR Phys. Solid Earth*, Engl. Transl., *10*, 654–659.

Wilson, M., and M. Monea (2004), IEA GHG Weyburn CO_2 monitoring and storage project summary report 2000–2004, paper presented at 7th International Conference on Greenhouse Gas Control Technologies, Pet. Technol. Res. Cent., Vancouver, B. C., Canada.

Wood, A. W. (1955), *A Textbook of Sound*, MacMillan, New York.

Yilmaz, O. (1987), *Seismic Data Processing*, Soc. Explor. Geophys., Tulsa, Okla.